Simulation Study of Magnetic Field Effects in the Pair Spectrometer Luminosity Detector for the ePIC Experiment at the Electron Ion Collider

by
Juan Diego Cristancho Guerrero

A thesis submitted to the Department of Physics,

College of Natural Sciences and Mathematics

in partial fulfillment of the requirements for the degree of

Master of Science
in Physics

Chair of Committee: Rene Bellwied

Committee Member: Gemunu Gunaratne

Committee Member: Claudia Ratti

Committee Member: Greg Morrison

Committee Member: Pablo Yepes

University of Houston
May 2025

DEDICATION/EPIGRAPH

"Science, my lad, is made up of mistakes, but they are mistakes which it is useful to make, because they lead little by little to the truth."

— Jules Verne, *Journey to the Center of the Earth*

ACKNOWLEDGMENTS

Firstly, this thesis would not have been possible without the support of my advisor professor Rene Bellwied and, an the opportunities given to me by Professor Pablo Yepes. I would like to express my gratitude for their guidance and support during this time.I am also thankful to the help that Dhevan Gangadharan and Aranya Giri provided as intelectual guidence being key pieces in the formulation and completion of this thesis.

In addition, I would like to express my appreciation to my friends Gustavo Valdivia, Alfonso Castillo, and Jeseleth Van Rose, who supported me in countless ways during this time—helping me grow academically, supporting me as a human being, and bringing light during uncertain times.

ABSTRACT

We aim to address the challenge of optimizing the magnetic field configuration that guides pair-produced e^+e^- from the conversion foil to the pair spectrometer trackers and calorimeters. This involves systematically exploring a range of tunable parameters that influence the acceptance rate, the efficiency with which both members of the pair are detected. Key parameters include the distance from the dipole magnet, the dimensions of the pair spectrometer, the magnetic field strength within the dipole, and the width of the photon beam.

The study is conducted within the DD4hep framework, which enables detailed simulation of the detector geometry and associated components. This facilitates analysis of particle trajectories and tracker acceptance in a realistic experimental setup. A significant challenge arises from the wide energy spectrum of Bethe-Heitler photons (0–18 GeV), which affects the pair acceptance for any given tracker configuration at the Electron-Ion Collider (EIC).

The ultimate goal is to develop a flexible suite of scripts and algorithms capable of fine-tuning the tracker acceptance based on adjustable design parameters. This approach allows adaptation to evolving experimental requirements and maximizes detection efficiency across the full photon energy spectrum. As a result, it contributes to reducing systematic uncertainties in luminosity measurements across different beam energies at the EIC.

TABLE OF CONTENTS

LIST OF FIGURES

1 Introduction

Nuclear matter exists in various forms, including protons, neutrons, atomic nuclei, neutron stars, and quark-gluon plasma. It is a highly intricate many-body system composed of quarks, antiquarks, and gluons, which interact through the strongest fundamental force—the strong nuclear force. To deepen our understanding of the role of quarks and gluons in nuclear matter, a cutting-edge accelerator, the Electron-Ion Collider (EIC), is being developed.

Although electron scattering has traditionally been a tool for studying nuclear structure, it may seem surprising that it can also serve as a precise probe for gluons and gluon-rich matter, despite gluons carrying no electric charge. However, both the photons exchanged in electron scattering and gluons can transform into quark-antiquark pairs, which can then interact via their electric or color charges. These interactions through intermediate quark-antiquark pairs are now well understood.

The EIC will represent a major advancement in experimental capabilities compared to previous electron scattering facilities. It will achieve collision energies and will outperform the former electron-proton collider HERA at DESY in Hamburg, Germany, by offering higher luminosity, enhanced polarization control, and unprecedented precision in exploring the structure and dynamics of nuclear matter. Some new aspects of the EIC compared to previous experiments are:

- providing spin-polarized proton and light ion beams to explore the correlations of gluon and sea quark distributions with the overall nucleon spin.
- heavy-ion beams to reach much higher gluon densities than with proton beams.
- extensive energy variability to map the transition in nuclear properties from a dilute gas of quarks and gluons to saturated gluonic matter.
- collision rates (luminosity) 100–1000 times higher, allowing unprecedented three-dimensional imaging of the gluon and sea quark distributions to explore correlations among them.

The EIC will facilitate electron-proton collisions within an energy range of 20 to 140 GeV. Its advanced detection capabilities will enable precise measurements of the energies and angles of final-state particles, such as the scattered electron and the hadronic remnants. These measurements will allow the determination of key variables, including x, Q^2, y and s. Here, x denotes the momentum fraction carried by the struck parton relative to the parent proton, while Q^2 represents the squared momentum transfer between the electron and proton, which is inversely related to the resolution of the interaction. The following subsections offer a concise overview of several key topics and challenges that the EIC is expected to address. However, one of the most profound questions—how mass arises within hadrons and, consequently, the visible universe—will be explored in greater detail in the next section.

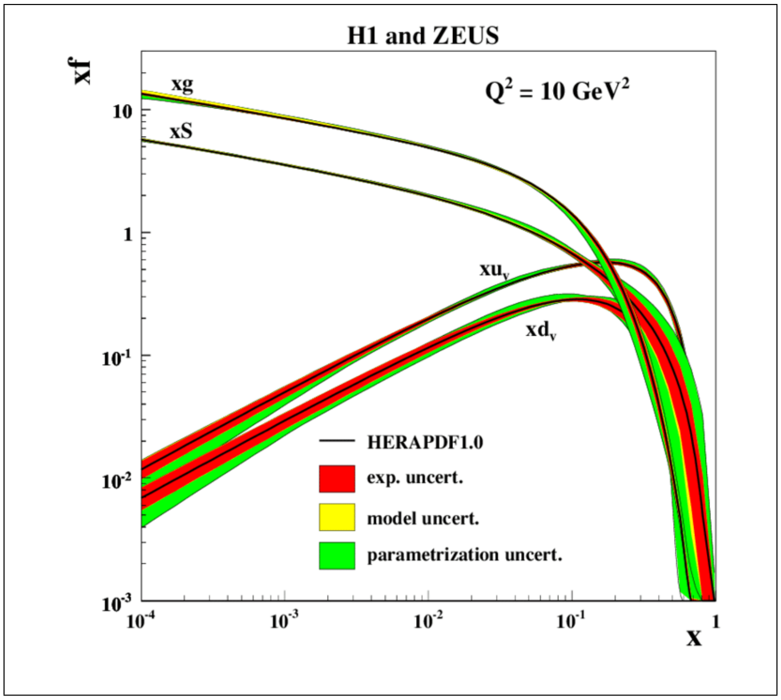

Figure 1: The parton distribution functions from HERAPDF1.0 (This is the Name associated with the PDF.), where we see the gluon, valence up and down quark and the sea of quarks as xS. Here the x axis is the momentum fraction of the parton, and the y axis is the product of the momentum fraction and parton distribution function which represents the momentum distribution function of the parton. [1]

1.1 Nuclear spin

For decades, nuclear physicists have sought to understand the origin of nucleon spin by analyzing its contributions from quark and gluon spin, along with parton orbital angular momentum. The total nucleon spin can be decomposed into its fundamental components, as expressed in Equation 1.

$$\frac{1}{2} = \frac{1}{2}\Delta \sum(\mu) + \Delta G(\mu) + L_{q+g}(\mu) \tag{1}$$

Here $\Delta \sum(\mu), \Delta G(\mu)$ and, $L_{q+g}(\mu)$ denote the contributions from quark and antiquark spin, gluon spin, and parton orbital angular momentum, respectively. However, the exact numerical values of $\Delta \sum$ and ΔG remain highly uncertain, primarily due to the lack of data on parton helicity (the projection of a spin vector in the direction of its momentum vector) distributions for $x \leq 0.005$.

In the 1980 the EMC experiment at CERN discovered that $\Delta \sum$ term accounts for only a small portion of the nucleon spin, emphasizing the need for further investigation. Subsequent fixed-target polarized electron/muon deep inelastic scattering (DIS) experiments, along with polarized proton-proton collisions at RHIC, have reinforced these findings, providing strong evidence for a nonzero contribution from orbital angular momentum. The EIC aims to greatly reduce the uncertainties in nucleon spin decomposition by delivering precise measurements across the full kinematic range, particularly in the region where $x \leq 0.005$. This will lead to a more profound understanding of the phenomenology of nucleon spin decomposition.

1.2 Nucleon structure.

Inclusive Deep Inelastic Scattering (DIS) has provided a one-dimensional perspective of the nucleon, but to capture the full 3D parton structure in momentum space, Transverse Momentum Dependent Parton Distributions (TMDs) are essential. TMDs offer valuable insights into the dynamics of nucleons by revealing the correlations between parton spins and their transverse momenta. The

Electron-Ion Collider (EIC), with its polarized beams and broad energy range, holds significant potential to enhance our understanding of TMDs by mapping the 3D momentum structure of nucleons for different quark flavors and gluons over a wide range x and Q^2

The EIC is ideal for studying TMDs as it enables the exploration of SIDIS (Semi-Inclusive Deep Inelastic Scattering) observables over a wide range in Q2 while covering the transverse momenta of final-state hadrons from non-perturbative to high perturbative values. The scale-dependence or evolution of TMDs as predicted in QCD is more complex than the evolution of 1D PDFs, making the EIC ideal for such studies.

The EIC has the potential to transform our understanding of the nucleon's 3D structure in momentum space by providing high-precision data over a wide range in Q^2 while covering the transverse momenta of final state hadrons from non-perturbative to high perturbative values. The study of TMDs at the EIC can reveal new insights into the dynamics of nucleons and provide a better understanding of QCD.

1.3 Nuclear modifications of PDFs.

Our understanding of nuclear parton distribution functions (nPDFs) is limited compared to our knowledge of parton distribution functions in the proton. Existing data on nPDFs comes from fixed-target experiments in a region of intermediate to high-x values. Data from hadronic collisions at the LHC have had little impact on extracting nPDFs. However, high-energy electron-nucleus collisions at the EIC will provide the capability to probe nuclear parton distribution functions (nPDFs) across an extensive range of Q^2, providing an unprecedented understanding of the collective effects that modify nuclear PDFs. To quantify how parton distributions in nuclei are modified, their ratio to parton distributions in the proton is plotted, normalized by the nucleus's atomic number. The deviation of this ratio from unity indicates that the nuclear parton distributions are not simple convolutions of those in the proton. The nuclear PDFs are determined through global fits to existing inclusive deep inelastic scattering data off nuclei, with structure functions $F2$ and F_L. Measuring F_L necessitates data collection at multiple center-of-mass energies. Additionally, charm production via photon-gluon fusion serves as a crucial probe of the gluon distribution at moderate to high x. As energy increases, the fraction of charm production also rises, providing a strong and independent constraint on the gluon content in nuclei at high x.

1.4 Gluon saturation QCD Molecule.

The EIC aims to explore the internal structure of nuclei in terms of QCD degrees-of-freedom and understand the formation of nuclei. It will be the first experimental facility designed to investigate the three-dimensional structure of sea quarks and gluons within a nucleus at low x. The nucleus serves as a distinctive QCD laboratory, offering a platform to uncover the collective dynamics of gluonic matter and investigate the quark-gluon foundations of short-range nucleon-nucleon forces within nuclear systems. Gluon saturation, a phenomenon where gluon density within a nucleus stops increasing at extremely high energies due to balancing gluon production and recombination, is a key feature of QCD, and the emergence of a momentum scale Q_S is known as the saturation scale. The Color Glass Condensate (CGC) is an effective field theory that enables computations of the dynamics of strongly correlated gluons. Its underlying dynamics using multiple experimental signatures, such as suppression of di hadron angular correlations, diffraction, and diffractive particle production in e+A scattering. Saturation models suggest that at the EIC, more than 20% of the cross-section will be diffractive, offering strong evidence for gluon saturation. An early measurement of coherent diffraction in electron-nucleus (e+A) collisions at the EIC could provide the first definitive proof of gluon saturation.

1.5 Transport of color charge through cold QCD matter.

In e+A scattering events, the virtual photon carries a large fraction of the electron's energy and interacts with a quark from a nucleon in the nucleus. The struck quark then traverses the nucleus, loses energy, and eventually hadronizes to form a color-neutral hadron. The location of the hadronization process—whether it occurs inside or outside the nucleus—is influenced by the quark's energy and the atomic number of the nucleus. If the virtual photon energy is high, the quark will produce a jet that can be measured experimentally to study the hadronic component in high-energy photon structure, gluon helicity in polarized protons, and parton distribution functions. Jet measurements offer valuable insights into QCD hadronization, shower development, and the effects of cold nuclear matter. Unlike leading hadrons, jets are complex structures with detailed internal substructure, preserving the history of multiple interactions with the target nucleus. Additionally, hadron measurements and heavy flavor production in reactions with nuclei of different sizes can provide further experimental avenues for understanding the transport properties of nuclear matter and cold-QCD effects of color charge. The EIC's variable energy and ability to "dial" the nuclear size will enable a systematic study of the emergence of jets and their internal spatial structure as an additional topic of interest.

1.6 Hadron Mass.

Chromodynamics is a gauge field theory that describes the strong interaction between quarks and gluons. As a scale-invariant theory, it predicts that there can be no bound states, which poses a problem for the existence of the universe. The Higgs mechanism, responsible for giving mass to fundamental particles, does not resolve this issue, as the masses of protons and neutrons are significantly greater than the masses of the light, up, and down quarks that the Higgs mechanism generates. However, in reality, composite Nambu-Goldstone(NG) bosons like pions are nearly massless, which effectively hides the strong interaction's mass scale.

The EIC is expected to make significant contributions in this area through five key experimental efforts:

- Measuring pion and kaon parton distribution functions (PDFs) and pion generalized parton distributions (GPDs).
- Measuring open charm production from pions and kaons will help understand the gluon (binding) energy in Nambu-Goldstone (NG) modes.
- Measuring the form factors of pions and kaons will help understand how mass is acquired

through Dynamical Chiral Symmetry Breaking (DCSB).

- Measuring the valence quark distributions in pions and kaons at large momentum fraction x will help explore the interplay between the strong force and the Higgs-driven mass generation mechanisms
- Fragmentation of a quark into pions or kaons to study the timeline analog of mass acquisition.

1.6.1 Pion (Kaon) PDFs and GPDs at EIC.

The masses of particles like the pion, kaon, and proton have been thoroughly studied to understand the contributions from quark and gluon energy, as well as quark masses. While the proton's mass is primarily attributed to the trace anomaly in QCD, the mass of the pion either has no contribution from the trace anomaly or experiences a cancellation of terms that guarantees the pion remains massless in the chiral limit.

To gain further insight into the contributions to particle masses, experiments have been proposed for the EIC. By measuring the pion and kaon structure functions over a large range of x_π and momentum-transfer squared, Q^2, it may be possible to extract valence quark, sea quark, and gluon distributions from projected EIC data. Additionally, measurements of the neutral-current parity-violating asymmetry could provide a further consistency check for the pion PDFs and enable u and s, $\bar{s}$ quark flavor separation at large x for the kaon.

A major motivation for these experiments is that the leading x-moment of the pion's (or kaon's) Generalized Parton Distribution (GPD) offers a way to probe the distributions of mass and momentum within the pion (or kaon).

1.6.2 Open charm production in Pion and Kaon.

One way to access gluon distributions is through open charm production, which allows for the measurement of gluon PDFs in the proton's meson cloud. At high momentum transfer squared scales (Q^2), it is expected that the gluon distributions in the proton will increase until a saturation scale is reached. However, in the chiral limit, there are still unanswered questions about the behavior of gluons in pions. For instance, it is unclear whether the gluons disappear or persist in the pion and whether cancellations keep the pion near-massless

1.6.3 Pion and Kaon Form factors.

EIC measurements will allow pion form factor studies to reach higher Q^2 values by analyzing the ratio of positively- and negatively-charged pions in quasi-elastic electron-pion scattering. The EIC's precise and systematic pion form factor dataset will enable a deeper investigation into the region where $F_\pi(Q^2)$ is influenced by emergent mass generation through Dynamical Chiral Symmetry Breaking (DCSB) and how it evolves with energy scale.

1.6.4 Quark fragmentation into Pion and Kaon.

The Electron-Ion Collider (EIC) will provide precision data on quark fragmentation into a pion or kaon as a function of z and transverse momentum k_T at large $z > 0.5$ and small $k_T < 1$ GeV. This data will test the aspects of QCD calculations that incorporate and express emergent phenomena, such as confinement, dynamical chiral symmetry breaking (DCSB), and bound-state formation.

2 Electron Ion Collider

The Electron Ion Collider (EIC) is a new particle accelerator planned to be built at Brookhaven National Lab in Long Island, New York, by the US Department of Energy. The Electron Ion Collider will study protons, neutrons, and atomic nuclei by colliding high-energy electrons with high-energy protons or ion beams. The EIC will be able to produce high intensity polarized electron and ion beams (reaching a polarization of 70% for both electron and ion beams). Some of the design specifications require:

- Luminosity up to 10^{33} to $10^{34} cm^{-2} s^{-1}$.
- contains more than one interaction region.
- ability to collide deuterons and heavy nuclei beams.

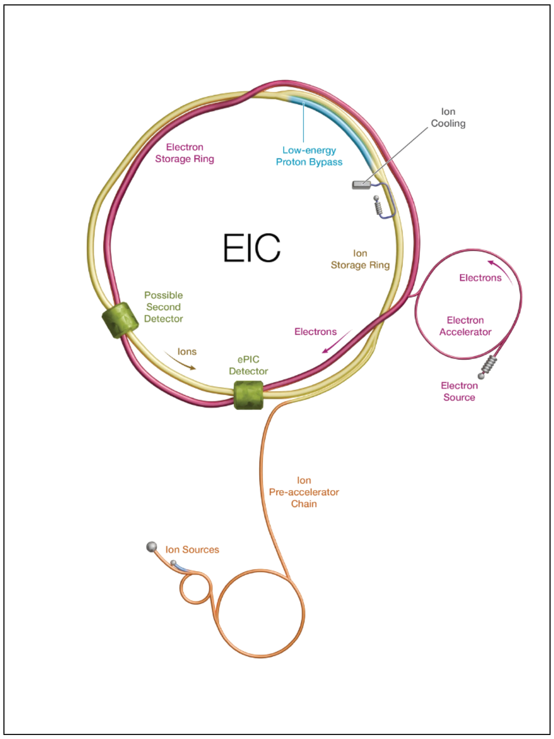

Figure 2: Schematic of the Electron Ion Collider. [2]

This new large-scale accelerator is the only facility planned to be constructed in the U.S. for the next decades, and it will be the largest and most advanced in the world. The creation of this machine is a joint effort from Brookhaven National Laboratory and Thomas Jefferson National Accelerator involving researchers from numerous universities and facilities from around the world.

2.1 Design Requirements

The success of the EIC depends primarily on the center of mass energy, luminosity, the lepton and ion polarization, and the accessibility to ion beams from deuterons to the heavier nuclei, complemented with two interaction regions and robust detectors.

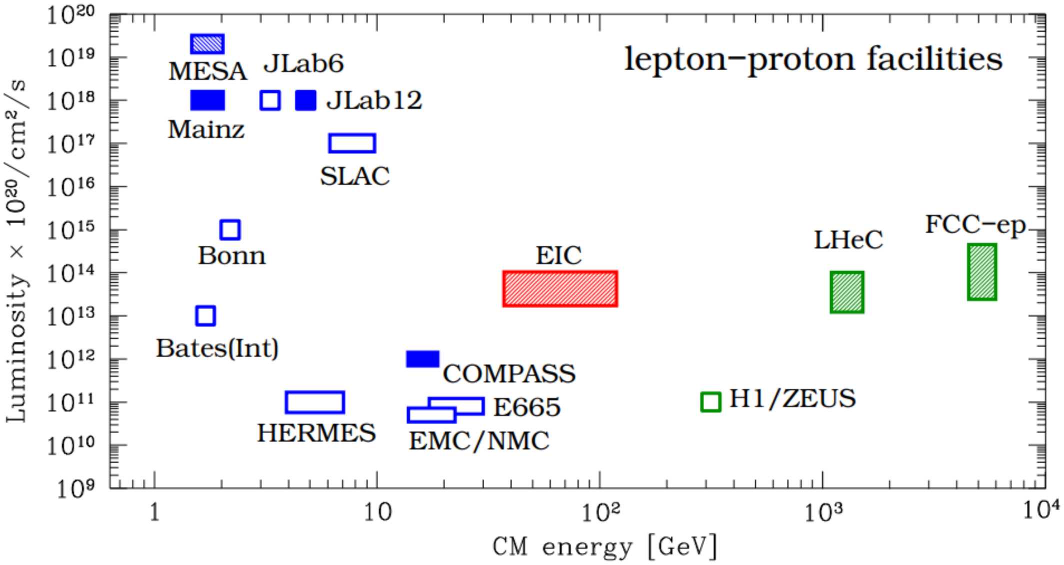

Figure 3: Luminosity vs. center-of-mass energy where the solid markers are the current experiments, the empty boxes are past experiments, and the shaded markers are the future facilities. [5]

1. **Center of mass energy:** To secure the kinematic reach required, it is necessary for the EIC to have a variable center of mass-energy $\sqrt{s} \sim$ 20-100 GeV that can later be upgraded to 140 GeV. This energy will provide enough kinematic reach to investigate the gluon regime.

2. **Luminosity:** The EIC is designed to reach a luminosity of $10^{33} cm^{-2} s^{-1}$ and $10^{34} cm^{-2} s^{-1}$. Note that with Hadron Cooling a luminosity of $10^{33} cm^{-2} s^{-1}$ generates an integrated luminosity of approximately $1.5 fb^{-1}$ per month. As archived by RHIC, here we assume a 60%

operation efficiency; if we do not assume hadron cooling, this percentage is reduced to 30%, where the average luminosity per fill is decreased to 70% of the peak luminosity. The benefit of obtaining a luminosity of $10^{34}m^{-2}s^{-1}$ is the ability to study spatial distributions of the proton polarized beams (quarks and gluons) for which measurements need an integrated luminosity of $100fb^{-1}$. It is also possible to make simultaneous measurements by choosing the correct beam species and beam orientation. These physics topics are discussed in the EIC white paper.

3. **Polarization Beams:** The EIC involves double spin asymmetries, which means that both electron and hadron beams are polarized, and single-spin asymmetries, which typically only requires the hadron beam to be polarized. The asymmetry for double spin dependence is $\frac{1}{P_e P_p \sqrt{N}}$ and for single spin is $\frac{1}{P\sqrt{N}}$. Measurements need transverse and longitudinal polarization, and the statistical uncertainty for spin asymmetries is directly correlated to the degree of polarization.

4. **Heavy Ion Beams:** Heavy nuclei Ion beams with high $\sqrt{s}$ (Lead, Uranium or Gold) will allow us to access high gluon densities and understand the propagation of colored particles in nuclear matter.

2.2 Detector Requirements

To generate precise measurements, the EIC requires being able to reconstruct kinematic variables with precision $(x, y, z, Q^2, W, \theta, \phi)$, across the forward, central, and backward regions, the first one being the direction on which the ion beam continues after the interaction point, the central region is where the main detector is located and the interaction occurs, and the backward region is found in the direction of the elctron beam after the interaction region. This generates heavy requirements on the detectors imposing conditions for the acceptance and the resolution of the measured quantities.

We will now summarize the detector requirements for successfully generating measurements at the EIC [2].

1. A 4π hermetic detector that contains low mass inner tracking.
2. The EIC detector must have moderate radiation hardness requirements.
3. Momentum resolution in the central detector ($\sigma_{pt}/pT(\%) = 0.05pT \otimes 0.5$).
4. Momentum resolution in the backward region with low multiple scattering terms ($\sigma_{pt}/pT(\%) = 0.1pT \otimes 0.5$).
5. The primary detector needs to cover the range of $-4 < \eta < 4$ for the measurement of electrons, photons, hadrons, and jets. It will need to be augmented by auxiliary detectors like a low-Q2 tagger in the far backward region and proton (Roman Pots) and neutron (ZDC) detection in the far forward region.
6. The components of an EIC detector will have moderate occupancy as the event multiplicities are low. However, specific components close to the beamline might see higher occupancies depending on the machine background level.
7. Excellent PID for $3\sigma\pi$/K/p separation up to 50 GeV/c in the forward region, up to 10 GeV/c in the central detector region, and up to 7 GeV/c in the backward region.
8. Hadronic resolution in the forward region ($\sigma(E)/E \approx 50\%/\sqrt{E} \otimes 10\%$).
9. Momentum resolution at forward rapidities ($\sigma(pT)/pT(\%) \approx 0.1pT\otimes$ (1 - 2)).
10. Impact parameter resolution for heavy flavor measurements ($\sigma_{xy} \sim 20/pT \otimes 5\mu m$).
11. Good electromagnetic calorimeter resolution in the central detector ($\sigma(E)/E \approx 10\%/\sqrt{E}\otimes$ (1-3)% at midrapidity).
12. Electromagnetic calorimeter resolution at backward rapidities($\sigma(E)/E \approx 2\%/\sqrt{E}\otimes$ (1-3)%).

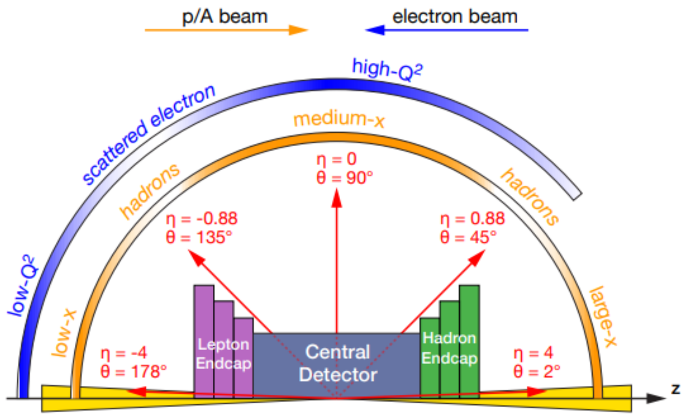

Figure 4: A schematic diagram illustrates the distribution of scattered leptons and hadrons across different x–Q^2 regions, mapped over the detector's polar angle and pseudorapidity coverage. [2]

2.3 Detector systems

The EIC detectors are necessary to make measurements describing the physical observables given by the theoretical calculations. The detectors used at the EIC will be large and sophisticated, which will be designed and constructed by multiple institutions and collaborations around the world. This experiment benefits from experience gained by previous efforts on creating e+p colliders like HERA in Germany. The detectors are planned to be located in the interaction regions, here the electron and ion Beams will collide. Since 2015, the US Nuclear Physics Long Range Plan suggested the implementation of multiple interaction regions, and the researchers planned for 2 EIC detectors. However, given funding constraints, only one detector is anticipated, this will be the ePIC detector that is shown in figure 4.

The EIC detector must be located in the interaction region, where, due to the high luminosity, the space is constrained. It is also required that it has strong integration of backward and forward detectors containing hermetic functionalities, helping the measurement of the energy-momentum four-vector of the particles in the final state within the energy range 10 MeV to 10 GeV

The EIC will have different detector systems consisting of a tracking and vertexing detector system, a particle identification detector system, a calorimeter detector systems, and auxiliary detectors. Concerning this study, we will mainly discuss the auxiliary detector system.

2.3.1 Auxiliary detector systems

Aside from the major central detectors, auxiliary detector systems are also needed in some parts of the EIC, (for example, electron and hadron polarimeters).

The EIC contains a far-forward and far-backward region. The far-forward region has silicon detectors in roman pots that are able to detect forward hadrons with high timing resolution and LGDADs (low-gain avalanche diodes). A zero-degree calorimeter will be used to detect the Neutrons and Low-energy photons located in the forward direction, this calorimeter also contains Electromagnetic calorimetry and Hadron calorimetry components. Technologies that are being used at ALice FoCal and the LHC Zero-Degree calorimeter are also considered.

This manuscript is focused on the far-backward region, where bremsstrahlung photons are detected in an electromagnetic zero-degree calorimeter or a pair spectrometer with the ability to determine the luminosity, which is an important variable as it is linked to the normalization of many observables. low-Q^2 electrons are tagged in the far-backwards detectors.

Additionally, in certain sections of the EIC, electron and hadron polarimeters will measure the polarization non-destructively with a precision greater than 1%.

A Compton polarimeter with a 20W laser diode produces the needed luminosity and repetition frequency for the electron beam. For the hadron beam, the polarimeters at RHIC are the starting point and blueprint of the ones that will be at the EIC.

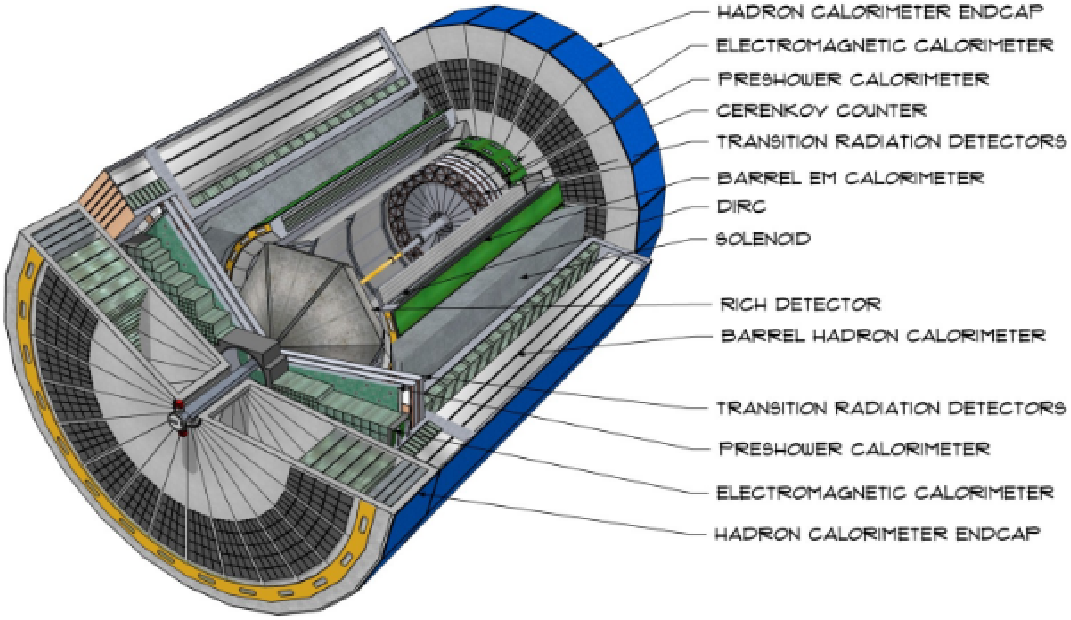

Figure 5: Concept of the EIC detector. [5]

3 Luminosity

Accurate knowledge of the luminosity is required to precisely determine a cross-section that corresponds to any process. Cross-section and luminosity are commonly used terms, they determine the likelihood of seeing interactions resulting in new particles.

Instantaneous luminosity (equation 4) helps us understand how tightly particles in a given space are packed; an increase in luminosity means a greater chance of particles interacting in a collision. A higher luminosity, for example, can be achieved by adding more particles to a beam or making the beam tighter.

$$L = \frac{1}{\sigma}\frac{dN}{dt} \tag{2}$$

Where L is the instantaneous luminosity, dN is the ratio of the number of events detected, dt is a period of time, and σ is the cross-section of a specific interaction.

There is also integrated luminosity, which corresponds to the total number of events during a period, normally the period of data taking. As an example, the Atlas experiment collected close to 150 femtobarns of data during the 2015-2018 LHC 13 TeV run, which corresponds to 16 million billion proton-proton collisions.

From a dimensional point of view, Cross sections are given in barns, while luminosity is given in inverse barns per second, meaning that the multiplication of these quantities will help use obtain the number of events per second.

$$\text{number of events per second} = crosssection(pb) * luminosity(pb^{-1}s^{-1})$$

3.1 Luminosity Calculations

By definition, we can now relate the cross-section and luminosity:

$$\sigma = \frac{N_{int}}{L_{int}} \tag{3}$$

Where N_{int} is the number of events that are observed for a given process during a time interval σ is the cross-section, and L_{int} is the integrated luminosity and is normally given in inverse picobarns.

Instantaneous luminosity is now then:

$$L_{inst} = \frac{dL_{int}}{dt} \tag{4}$$

In order to be able to perform measurements, we need to change these equations. At HERA, they use a measured rate R, which is the photons obtained from the known bremsstrahlung process $ep \to ep\gamma$, where the energy spectrum of this process is described by the Bethe-Heitler formula, which will be shown later in this manuscript.

We then obtain the equation:

$$L_{inst} = \frac{R}{fA\sigma} \tag{5}$$

Where σ is the bremsstrahlung cross-section, R is the rate of photons created over the same energy interval, f is the fraction of photons that convert to electron pairs for this case in the material upstream of the magnet and A is the acceptance, which represents the photons of interest whose converted electrons are able to trigger both pairs of tracker in other words, it the probability that both e^+e^- are observed in the spectrometer.

The lack of precision of A generates uncertainty in the measurements; this quantity is required for the luminosity and has two main issues.

1. photons that are removed from the edges of the bremsstrahlung beams by the obstacles upstream of the luminosity system.
2. the number of converted pairs e^+e^- that are accepted into the fiducial area of the trackers.

The second on this list is the main focus of this thesis, and the process of correctly determining the fiducial areas and the Acceptance will be explained in more detail.

3.2 Photon Luminosity Measurements

The luminosity measurements are done in the far-backward location of the experiments, the depiction or schematic of this section of the Electron Ion collider is shown in fig.6 where, the horizontal axis is aligned with the beam direction at the collision point, which is the path along which photons from e+p and e+A interactions will travel. These photons primarily originate from the bremsstrahlung process, which is used to determine luminosity.

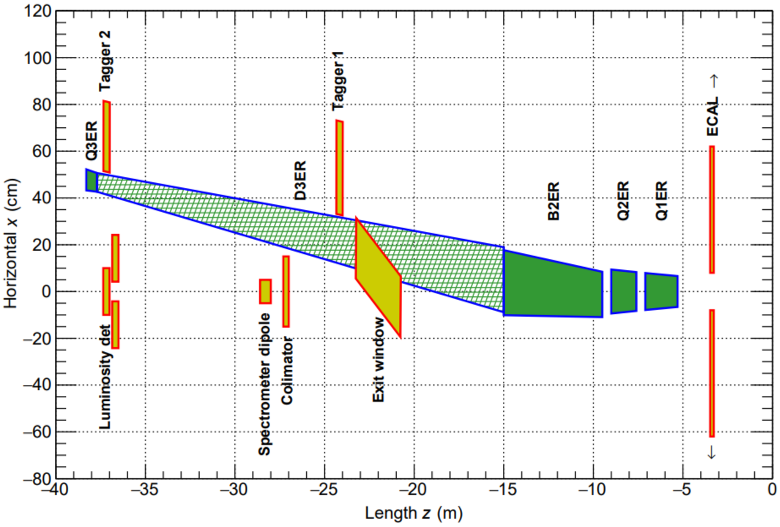

Figure 6: The trajectory of the electron beam downstream from the interaction point. Beam magnets are depicted in solid green, drift spaces in hatched green, and detectors and other components are shown in red and yellow. [2]

In the lower left corner of the figure, possible instrumentation for measuring luminosity is depicted. Bremsstrahlung and low-Q^2 processes also produce electrons with slightly lower momenta than the beam energy. These electrons are deflected from the beam path by lattice dipoles and can be detected by taggers, as shown in the upper left of the figure. This section will provide an in-depth examination of a luminosity monitor, as well as a tagger designed to capture electrons from bremsstrahlung and low-Q2 events.

3.2.1 Bremsstrahlung radiation

The bremsstrahlung process $e + p \rightarrow e + p + \gamma$ was successfully employed by the HERA collider experiments for luminosity measurements. This process has a well-established QED cross-section, which is large, reducing theoretical uncertainties and resulting in negligible statistical uncertainty. Consequently, the scale uncertainty of the luminosity is primarily determined by the systematic uncertainties involved in counting bremsstrahlung events. The ZEUS collaboration at HERA-II achieved a luminosity measurement with a 1.7% scale uncertainty. Their experience suggests areas for improvement, such as a better understanding of the acceptance of photons.

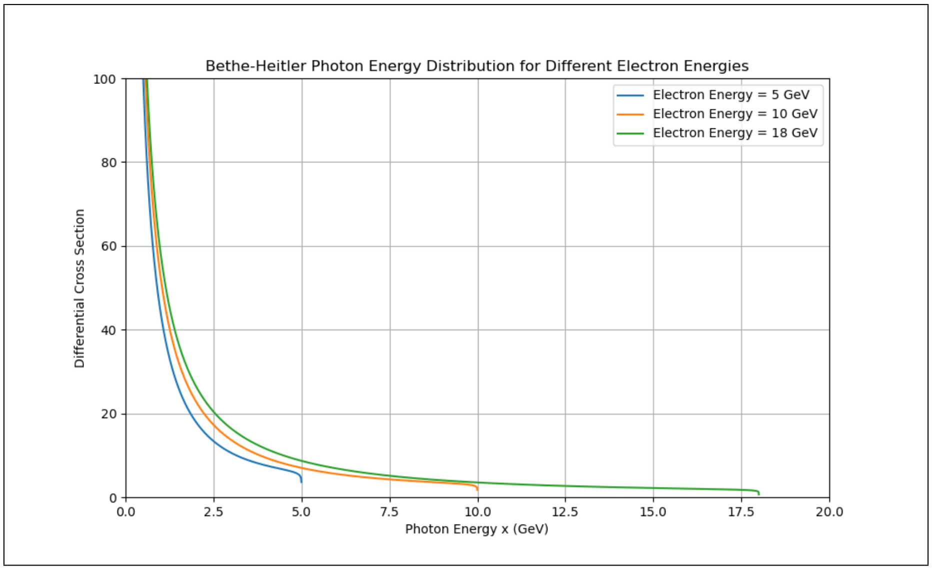

Figure 7: Bethe-Heitler curves for 3 electron beam energies 5Gev, 10Gev, 18Gev

At the EIC we expect three electron beams, with energies 5GeV, 10GeV, 18GeV and in figure 7, you can see the bremsstrahlung spectrum for the given beam energies.

3.2.2 Photons in the far backward region.

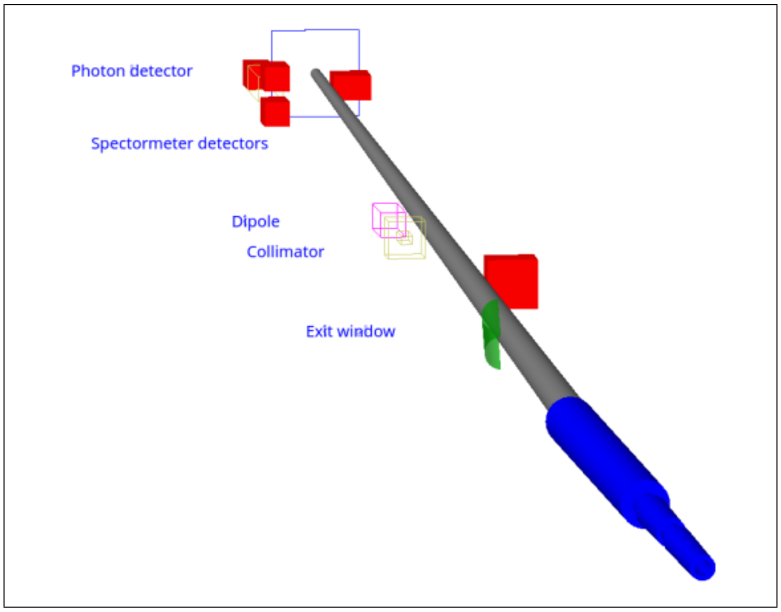

Figure 8: Geant4 schematic of the bremsstrahlung photon detector implementation. [2]

Figure 8 full schematic of the bremsstrahlung photon detector region of the Electro Ion Collider, where we see the components starting from the exit window all the way to the photon detector. Figure 9 shows the last portion of the photon detector with the sweeper magnet, dipole magnet, calorimeters, and trackers. For this thesis, we want to focus on the spectrometer detector system and the dipole magnet. Figure 11 shows a more zoomed-in version of the components of interest, these being the dipole magnet and the set of trackers, also adding the calorimeters behind these trackers. The figure also shows the current dimensions that were used for the simulations and the overall setup, where we see that the distance on the z axis from the dipole magnet and the trackers is 389cm, and 399 cm respectively and we are expecting the trackers to be located at 6.7cm from the y=0 location and have a length of 20cm.

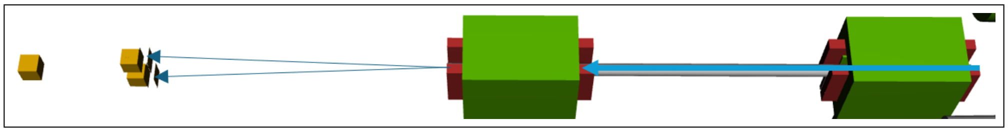

Figure 9: Schematic of the photon luminosity setup at the EIC, from the sweeper magnet (green box on the right) to the calorimeters and trackers on the left. In the middle, we see the dipole field as a green box.

The components are in the backwards direction along the zero-degree photon line. The most straightforward approach for detecting bremsstrahlung involves positioning a calorimeter at zero degrees along the electron trajectory and counting the resulting photons. However, this way the calorimeter will be exposed to the direct synchrotron radiation fan and has to be shielded, impacting the energy resolution. This creates a rough lower energy threshold for photons, typically around 0.1-1 GeV, below which the calorimeter becomes ineffective in detecting them. For the EIC luminosity, we expect a mean number of photons per bunch crossing of over 20 for electro-proton scattering, however, this number increases with Z^2 of the nuclear beams. In contrast, at peak HERA luminosities, the photon calorimeters were capable of detecting 1-2 photons per bunch crossing. The distribution of the per bunch energy is proportional to the number of per bunch crossing photons. Counting bremsstrahlung photons essentially becomes an energy measurement within the photon calorimeter, bringing with it the associated systematic uncertainties that accompany this type of measurement.

An additional method for counting bremsstrahlung photons and the main topic of this thesis, is to use a pair spectrometer (This is also used by the Zeus collaboration at HERA). A number of e^+e^- pairs are created from photons in the vacuum chamber exit window. Then a dipole magnet splits the pair, directing each particle to hit a separate tracker placed next to the unconverted photon path. This is the setup that we see in Figure 11. This configuration provides several benefits compared to a zero-degree photon calorimeter:

- This configuration avoids the synchrotron radiation fan.
- The exit window reduces the conversion fraction rate.

- This configuration generates a well-defined low-energy cutoff in the photons, which has a direct dependence on the magnitude of the dipole field and the spectrometer position.

The adjustable factors in the last two points, such as the dipole field strength, conversion fraction, and calorimeter positions, can be optimized to limit the rate to around or below one e^+e^- pair coincidence per bunch crossing, even at the expected EIC luminosities. As a result, the bremsstrahlung photon count is essentially the detection of e^+e^- coincidences within a pair spectrometer, requiring only corrections for pileup effects.

The rate in the spectrometer is directly linked to the fraction of photons that convert into e^+e^- pairs, imposing strict requirements on the photon exit window. The window must have a well-defined material composition, along with a precisely measured and consistent thickness along the photon's path.

Both luminosity devices require calorimeters for triggering and energy measurement purposes. Given the high event rates, the design must be radiation-resistant, particularly for the zero-degree calorimeter, which also needs protection from synchrotron radiation. In addition, the spectrometer needs precise position detectors to track the e^+e^- particles. When combined with the calorimeter's energy data, this enables the reconstruction of the converted photon trajectories. The distribution of these photon positions is necessary for accounting for photons that are lost outside the detector's aperture and acceptance range.

3.3 Acceptance

Acceptance is defined as the fraction of converted photons upstream of the magnet for which the pair e^+e^- are admitted into the Trackers.

The acceptance has a strong dependence on z, which represents the fraction of the photon energy carried by one of the electrons. This distribution has the shape:

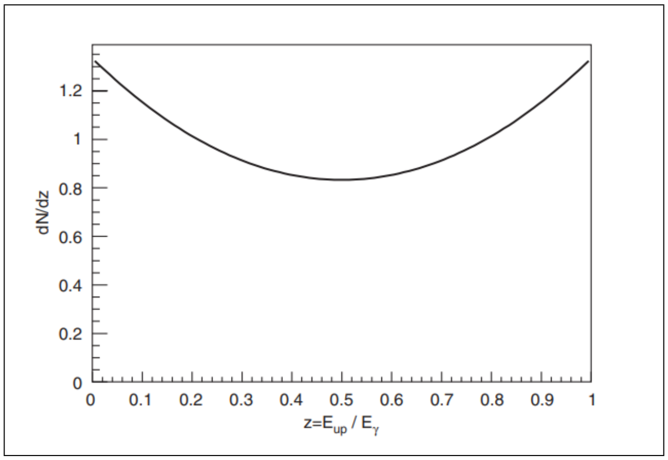

Figure 10: Shape of the distribution of the fraction of the photon energy transferred to one of the electrons after conversion. [4]

From Figure 10, we see that most of the acceptance depends on z and E_γ. Now, let us consider a photon traveling along the beam axis located in the middle of the trackers, meaning y=0. Each electron will then acquire the transverse momentum in the opposite direction from the transverse field.

$$P_T = 0.3 \int B_x dz \tag{6}$$

For an electron with momentum p, the selection in the magnetic field can then be approximated to:

$$y = l\frac{P_T}{p} \tag{7}$$

Where:

- l is the distance from the center of the magnet to the trackers.
- P is the momentum
- p_T is defined in equation 6

We will obtain acceptance when the y values for the pair e^+e^- are both in the region where they can be admitted into the trackers. We can now define the fraction of the photon energy acquired by the electron that is deflected upward as

$$z = \frac{p}{E_\gamma} \tag{8}$$

This means that the fraction acquired by the electron deflected in the downward direction is 1-z of the photon energy.

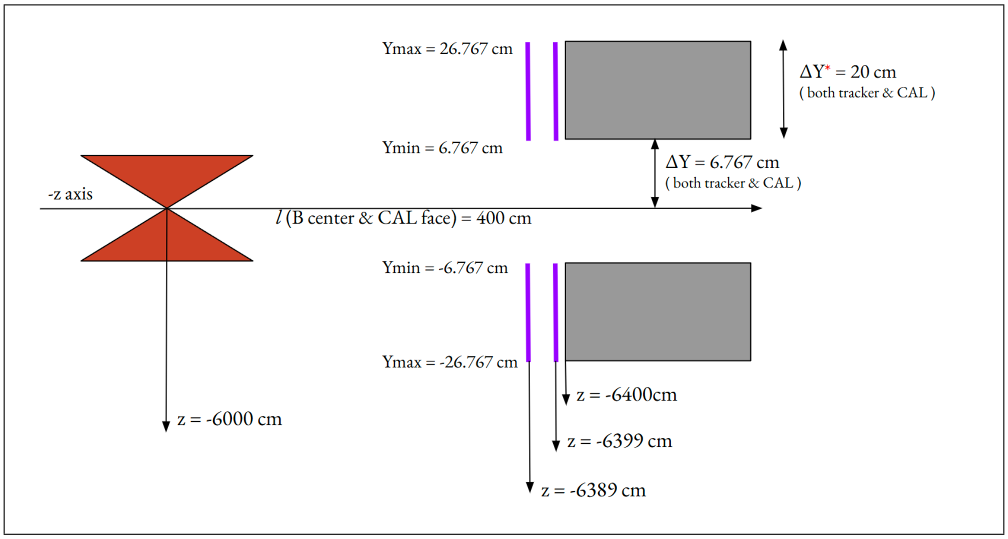

Figure 11: The spectrometer setup at the EIC with the dimensions used for the simulations.

Finally, we can now call the location of the electron as y_{up} for the upper tracker and y_{dn} for the lower tracker.

$$zE_\gamma = \frac{lp_T}{y_{up}} \tag{9}$$

$$(1-z)E_\gamma = \frac{lp_T}{y_{dn}} \tag{10}$$

From these equations, we can delineate what is called the fiducial area, this being the area for which a given photon energy will produce a pair e^+e^- that can be accepted into both trackers.

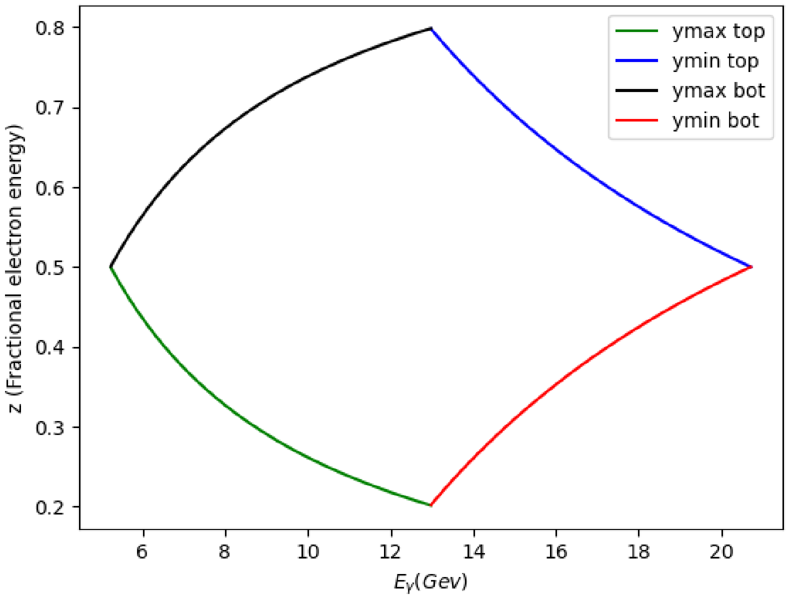

Figure 12: Fiducial area created from the trackers.

The curves in Figure 12 are the limits created by the size of the trackers. They are created by keeping one of the equations, 9 or 10, fixed and changing the other one from ymin to ymax of the dimension of the trackers, which can also be seen in Figure 11. Later in this thesis, we will describe its properties and how it changes with respect to the parameters used in the simulation.

The spectrometer's ability to accept bremsstrahlung photons based on their energy is shaped by the configuration depicted in Figure 11. This depends on factors such as the distance between the dipole magnet and the spectrometer detectors, the magnetic field of the dipole, and the vertical placement range of the up and down detectors along the y-axis.

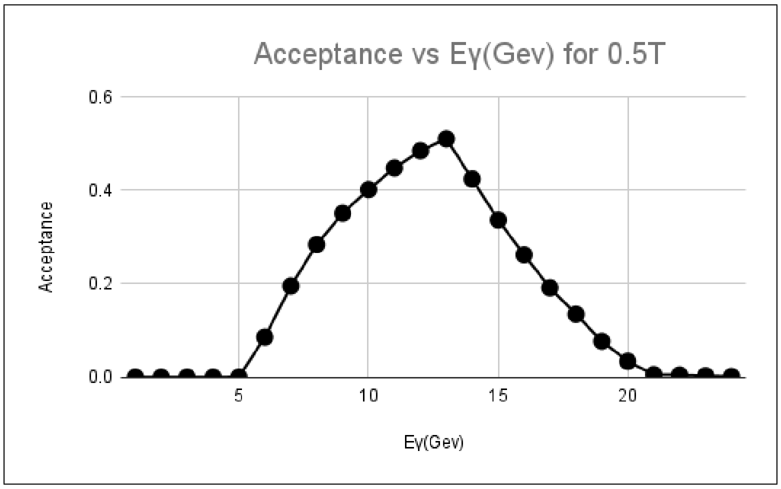

Figure 13: Example of acceptance curve obtained from simulations

Figure 13 shows the acceptance as a function of the generated bremsstrahlung photon energy. The acceptance is calculated as the fraction of events in which both the up and down detectors register a set number of pairs entering the trackers.

Both spectrometer detectors span the minimum and maximum positions along the y-axis, as shown in Figure 11. The requirement for coincidence detection limits the z-range within which the spectrometer can detect the converted photon. The acceptance at a given E_γ is then determined by integrating $\frac{dN}{dz}$ over this z-range, with the results displayed as a solid line in Figure 13. There is a good match between this model and the full Geant4 simulation. This approach can be used to fine-tune the magnetic field of the spectrometer dipole magnet to optimize the coincidence detection rate. Each electron beam energy will require its own specific magnetic field setting.

4 Simulation Toolkit

To simulate the events occurring in the Electron Ion Collider, multiple software and toolkits are used to generate the geometry, the detectors, and the particle behavior. This includes the use of multiple coding languages like Python and C++, and also the implementation of toolkits like Geant4 and DD4hep.

4.1 Geant4

Geant4 is a software toolkit designed for simulating how particles or radiation interact as they pass through matter. With Geant4, users can build applications to model various setups, detectors, and radiation sources, while capturing specific physical outcomes resulting from the interactions between source particles, secondary particles, and the materials within the setup.

Geant4 offers comprehensive tools for simulating particle transport. It enables users to:

- Identify points and trace particle paths within that model.
- Build a geometric model using various shapes and materials.
- Simulate the effects of physical interactions and produce secondary particles.
- Visualize the geometry of the setup and the paths of particles traveling through it.
- capture specific data as tallies or create hits to simulate detector responses.
- interact with the application through an adaptable terminal or graphical interface.

Geant4 provides a comprehensive range of physics processes for simulating electromagnetic, strong, and weak interactions of particles with matter. These processes cover an energy spectrum starting from milli-eV for thermal neutrons, eV for electrons, and typically keV for hadrons, extending up to hundreds of GeV and even partially reaching 100 TeV. For each interaction type, a full set of physics models is available. Additionally, users can select from different modeling approaches, with pre-configured options known as physics lists ready for use.

4.2 DD4hep

DD4hep is a software framework designed to provide a comprehensive solution for complete detector descriptions, including geometry, visualization, materials, alignment, readout, and calibration, throughout the entire experiment life cycle—from detector concept development and optimization to construction and operation. It ensures a consistent and unified representation of detector information for various tasks, including simulation, reconstruction, and analysis.

The primary motivation behind the DD4hep package is to create a toolkit that handles all aspects of detector description across all stages of an experiment. It was developed based on insights from the LHCb experiment and advancements within the Linear Collider community. DD4hep integrates pre-existing, widely adopted software into a unified, versatile framework for detector description. Its core components include the ROOT geometry package for constructing and visualizing geometry and the Geant4 simulation toolkit, which DD4hep can interface with to simulate detectors in complex designs.

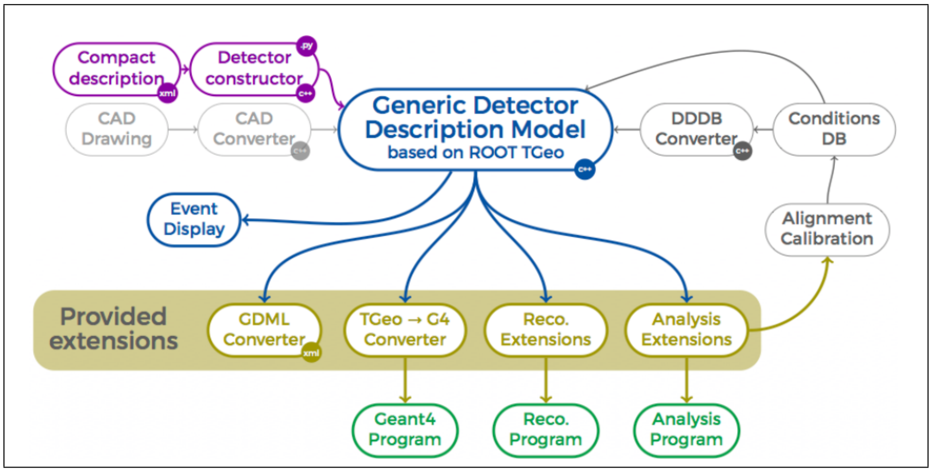

Figure 14: DD4hep detector geometry toolkit. [3]

5 Results and analysis

5.1 Motivation

Considering the Electron-Ion Collider is currently in its pre-build stage, it is crucial to find the optimal setup, such that it would work as intended after the building phase. We are interested in the far backward region, mainly the pair spectrometer that is found at the bremsstrahlung photon detection section. This thesis intends to understand the behavior of the acceptance region at the Electron-Ion collider and give suggestions regarding the optimal placement of the trackers, and what is expected if modifications to the setup are made.

5.2 Simulation procedure

Multiple scripts, software, and toolkits are used to produce the results that are shown in this thesis, I will now try to summarize the steps such that there is a better understanding of what is required to produce the results. All of the simulations are produced on Linux.

1. Firstly, we want to generate a "Create gen file", this file contains the parameters that we want in the initial state of the particles, we can impose the initial position of the particles, the number of desired particles, and the energy distribution of the e^+e^- pair splitting.

2. Now we grab the "create gen file" and simulate the events. This is done using dd4hep, which already contains all the detector aspects in the Electron-Ion Collider, and is able to reproduce the behavior of the events from the initial state until the particles enter the multiple detectors. In this portion of the process, we can specify the number of events that we want to simulate from the batch of particles we generated at the start.

3. The second step generates a pool of data. We want to filter this data and grab only the necessary. This is done by creating an analysis plugin which goes inside the simulation data, selecting the aspect that we are interested in, and saving it in a root file as trees and branches.

4. Finally, we can analyze and manipulate the data. For this specific project, a set of Python

scripts was created. This script goes inside the root file to grab the data and then manipulates it to, in this case, find the number of pairs e^+e^- that entered the spectrometer. Then the scripts return a root file containing the analyzed data and showing the number of particles that entered each of the trackers.

At each one of these steps, multiple parameters can be changed to generate a different outcome. However, the original geometry and dimensions of the detectors have to be modified inside the dd4hep scripts and compiled before running this procedure.

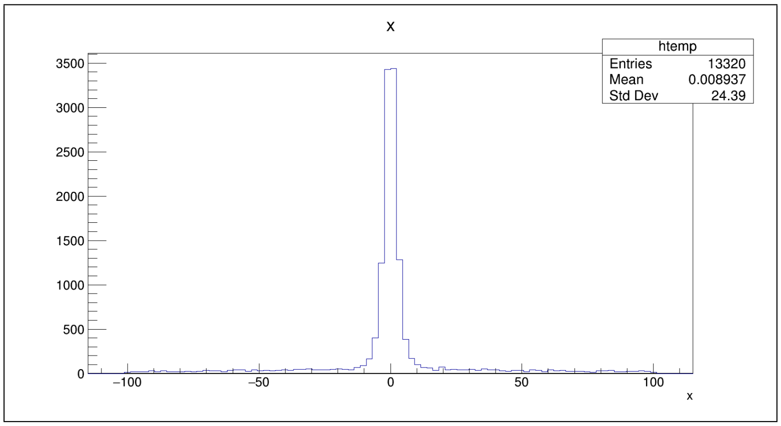

Figure 15: Histogram of the X position, where the y-axis shows the number of entries and the x-axis represents the X position (in millimeters) where electrons enter the spectrometer.

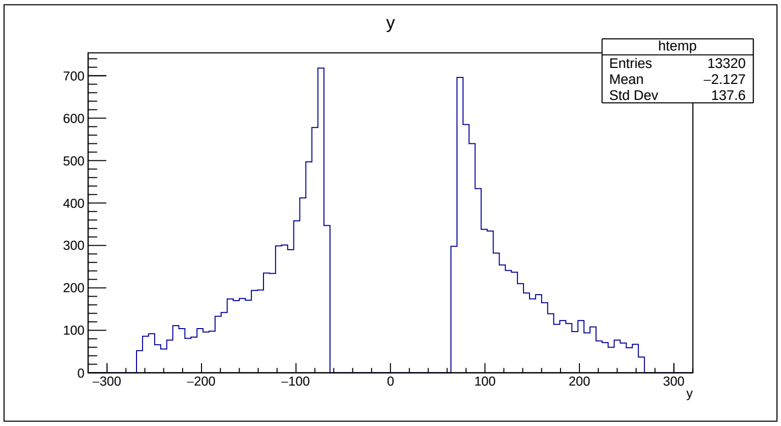

Figure 16: Histogram of the Y position, where the y-axis shows the number of entries and the x-axis represents the Y position (in millimeters) where electrons enter the spectrometer.

Here we see an example of how the distribution looks inside the root file, where the first figure, figure 15 shows the distribution of overall hits in the x position where, as expected most particles enter the trackers near the x=0 position since the magnetic field is a dipole field that splits the particles along y axis. In contrast, Figure 16 shows the number of particles hit with respect to the y position, where we see that most of the particles are entering the trackers near the ymin position. This means that the magnetic field inside the dipole magnet is not causing a big enough displacement for the energy of the events generated. These results are for five thousand events with a magnetic field of 0.25T and a constant photon energy of 7 GeV. In order to increase the number of pairs of particles entering both trackers (acceptance rate) we desire to move the peaks in Figure 16 to the center of the trackers, which will be closer to the 150mm to 200mm for the top tracker and -150mm to -200mm for the bottom tracker.

5.3 Analysis

The analysis will be done for 3 combinations of magnetic fields in the dipole magnet: 0.25T, 0.5T, and 0.75 T. Attempts with magnetic fields of higher magnitude were made, but the results obtained were highly suboptimal and not worth considering.

5.3.1 Acceptance regions

$$zE_\gamma = \frac{lp_T}{y_{up}} \tag{11}$$

$$(1-z)E_\gamma = \frac{lp_T}{y_{dn}} \tag{12}$$

$$P_T = 0.3 \int B_x dz \tag{13}$$

The acceptance region can be found by using equations 11 and 12. From these equations and using the dimensions and variables from the simulations, we obtain the acceptance area:

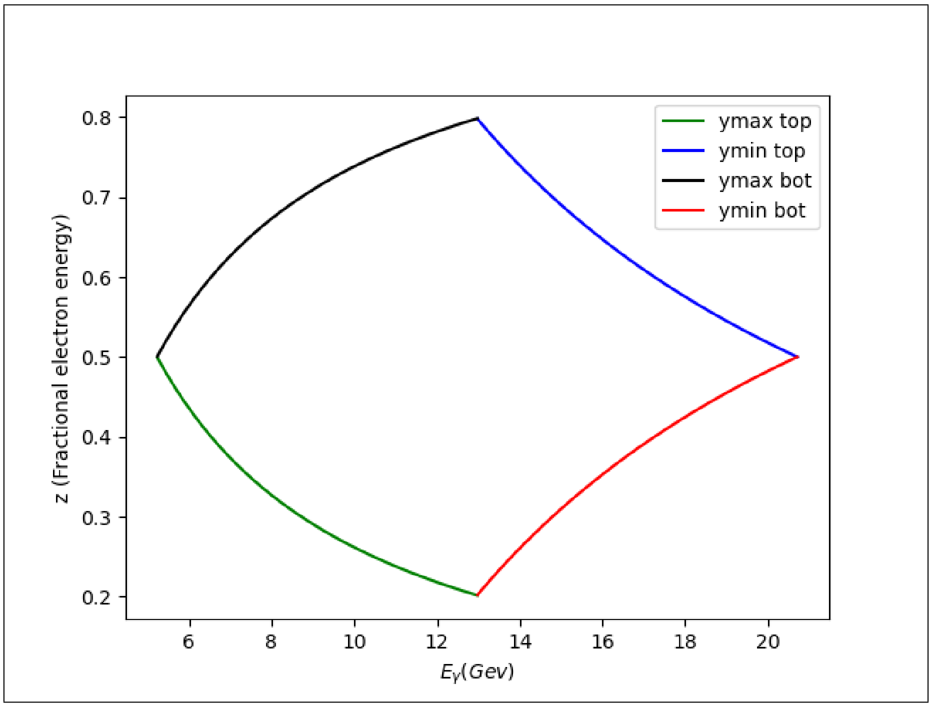

Figure 17: Fiducial area of a tracker located at 3.89 m away from the center of the dipole magnet.

This region is obtained by keeping one of the equations 11 or 12 at a fixed value of y and iterating over the second equation from ymin to ymax. The black and red curves are done by keeping the y value of the bottom tracker fixed and the other two curves require the same condition for the top tracker. The other variables are:

- ymin=0.06767 m
- ymax=0.2676 m
- l=3.89 m
- B=0.5 T
- dz=1.2 m

- p=0.18

- step size = 0.001

This will be our starting point and represents the acceptance or fiducial area of the pair spectrometer located at a distance l=3.89 meters away from the center of the dipole magnet. We see that the curve starts at around a photon energy of 5.5 GeV and goes all the way to 20 GeV, with the peak being near the 13 GeV region.

Now we want to compare the theoretical values to the simulated results. Using equations 9 and 10 we can find the exact values of the minimum value of the photon energy, maximum value and the peak of the acceptance, this gives us.

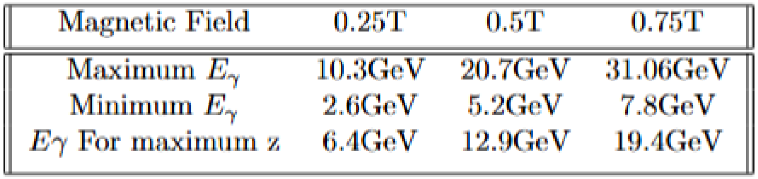

Magnetic Field	0.25T	0.5T	0.75T
Maximum E_γ	10.3GeV	20.7GeV	31.06GeV
Minimum E_γ	2.6GeV	5.2GeV	7.8GeV
$E\gamma$ For maximum z	6.4GeV	12.9GeV	19.4GeV

Figure 18: Table with the maximum, minimum, and peak z E_γ values

Using the procedure described in section 4.2, we can now generate simulations to find the acceptance curve and compare them to the theoretical values. The datapoints are generated by simulating five thousand events with a constant photon energy and then calculating the acceptance value of this run.

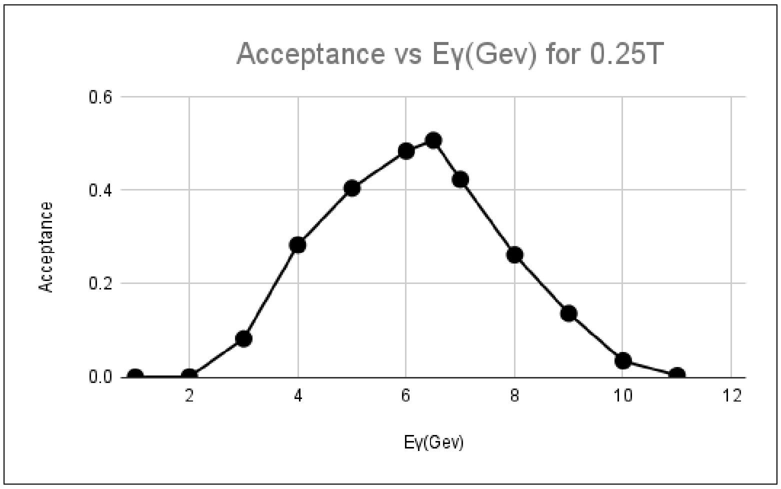

Figure 19: Acceptance vs E_γ for 0.25 T

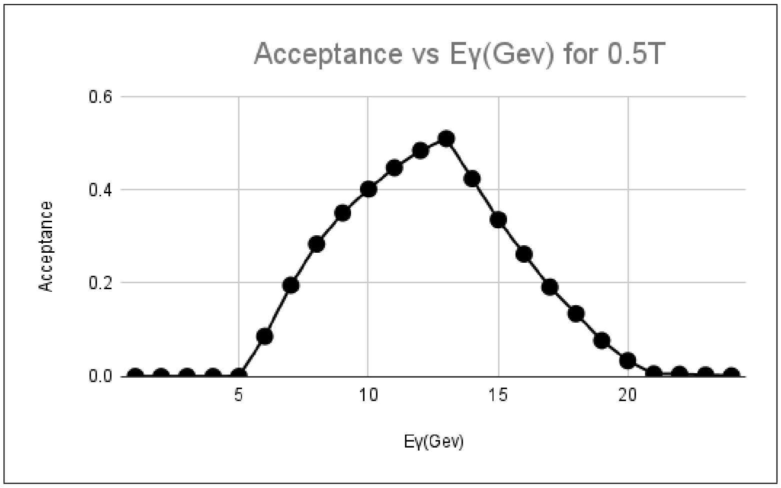

Figure 20: Acceptance vs E_γ for 0.5 T

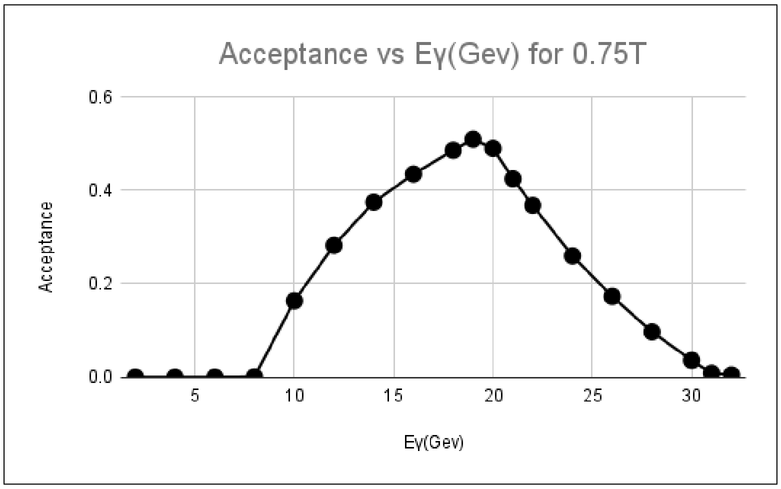

Figure 21: Acceptance vs E_γ for 0.75 T

All of the curves have been normalized with respect to the number of events simulated. We see that the simulated values and the theoretical values both match, meaning that the computational setup and algorithms created both agree, and we can continue to produce results using them.

5.3.2 Acceptance Regions for tracker and calorimeter at different magnetic fields.

We can now check how the Acceptance region behaves with respect to the location of the two pair spectrometers and the front of the calorimeter. The distance to tracker one is 3.89m, then 3.99m to tracker two, and 4m to the calorimeters. In the following graphs tracker 1 is in green, tracker 2 in blue, and the calorimeter in dotted yellow. Since the difference in length between the second tracker and the front of the calorimeter is only 1 cm, the change in the fiducial area is small but enough to see the displacement of the area.

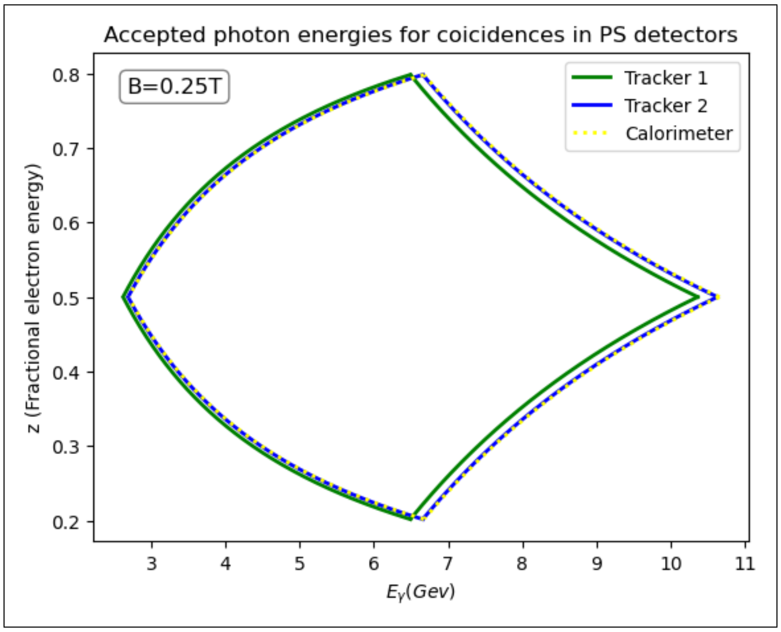

Figure 22: Acceptance vs E_γ Gev for 0.25 T for the trackers and front of the calorimeter.

We see that the region starts close to 3 GeV and goes to 11 GeV, and the peak is around 6.5 GeV, which for tracker one is within the values given by the theoretical results (figure 18).

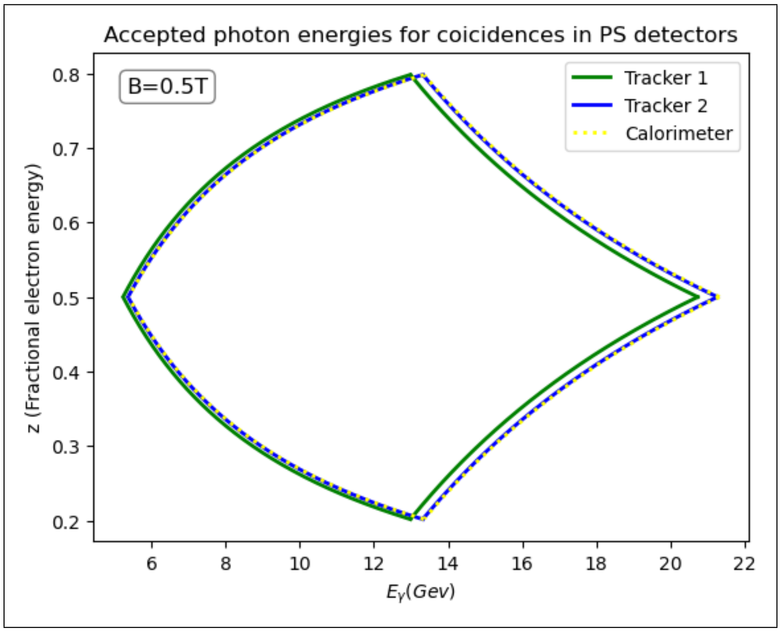

Figure 23: Acceptance vs E_γ Gev for 0.5 T for the trackers and front of the calorimeter.

Here, the region starts at 5.5 GeV and ends at 21 GeV with the peak at 13 GeV.

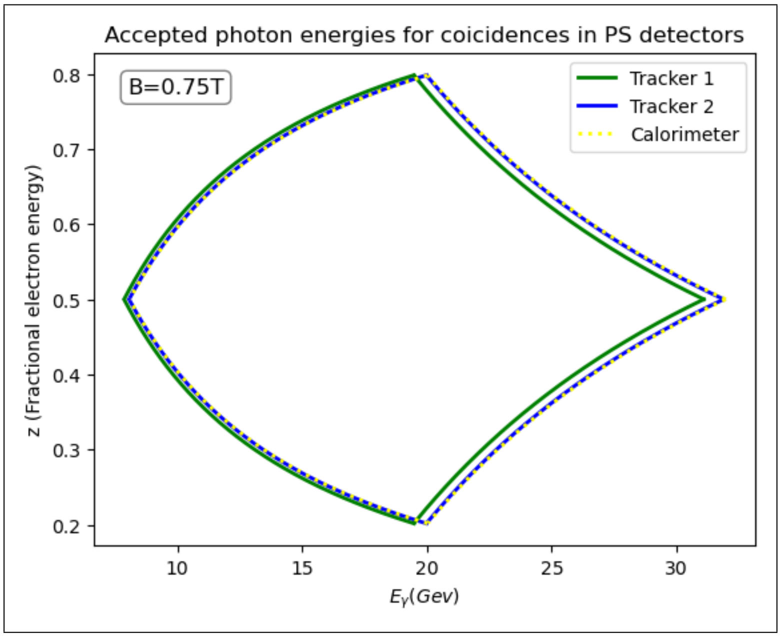

Figure 24: Acceptance vs E_γ Gev for 0.75 T for the trackers and front of the calorimeter.

For the last plot, we see that the fiducial area goes from 9 GeV to 30 GeV with a peak at around 20 GeV.

Overall, we see that the behavior of the fiducial area with respect to the distance from the calorimeters shifts the acceptance area to the right, admitting higher energy electrons, but ignoring a portion with lower energy. Finally, there is a more prominent change of the fiducial area with respect to the magnitude of the magnetic field in the dipole magnet. When the magnetic field is increased, the fiducial area grows, accepting a larger amount of energy values, however, the lower values of energy are not included inside the acceptance area. We do not want the option with the greater fiducial area; instead, we desire that the energy values of the bremsstrahlung photons are included.

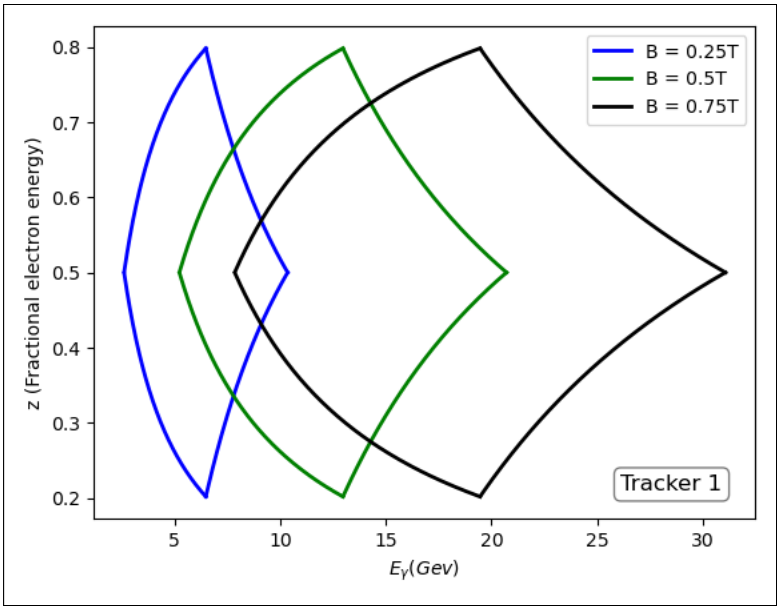

Figure 25: Acceptance area with respect to the magnetic fields

There is a clear correlation between the size of the acceptance area and the magnitude of the magnetic field. However, given the expected behavior at the Electron Ion Collider, we do not expect the bremsstrahlung photons to have an energy higher than 18 GeV, meaning that the use of the 0.75T magnetic field is not optimal for the current setup. Note that here we have maintained a constant distance to the dipole magnet, therefore, a magnetic field with 0.75 T could be used if other parameters are changed, mainly the position of the tracker, which ultimately will depend on the amount of space available inside the far backward region which dictates where we can place the trackers, and allowing us to the change the vertical and horizontal placement of the detectors opening a new set of possible values for the magnetic field.

5.3.3 Change in the acceptance region concerning the tracker size.

For this section, we want to analyze how the fiducial area changes with respect to the tracker size, this is done by keeping the tracker in a fixed position and then changing its size by bringing one of the edges closer to the other one. For example, we want to keep the ymax value fixed at $ymax = 0.2676$ m and bring the $ymin$ value, which represents the lower part of the tracker, closer by 5 cm and 10 cm.

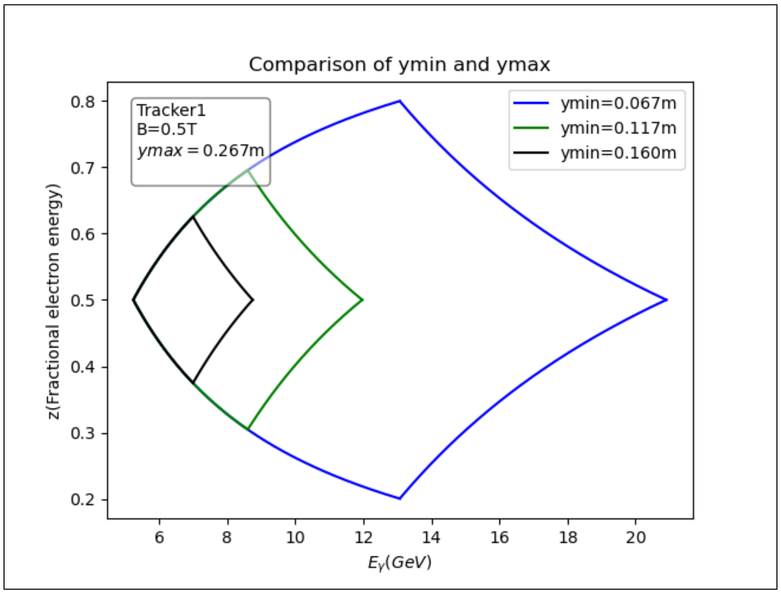

Figure 26: Acceptance region obtained by keeping ymax=0.2676 m and moving ymin

Here we see how changing the *ymin* value of the tracker greatly impacts the size of the fiducial area, lowering the higher energy accepted considerably.

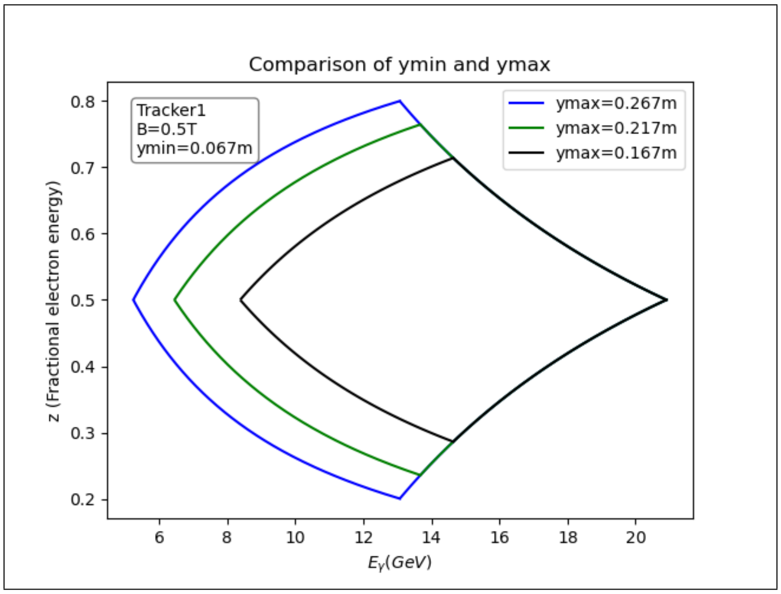

Figure 27: Acceptance region obtained by keeping ymin=0.0676 m and changing ymax

From the figures in this section, it becomes clear how the edges of the tracker are connected to the fiducial area. *ymin* directly affects the higher energy portion, and the opposite behavior is true for *ymax*. This is the expected behavior since we know that the electrons with higher energy will ultimately enter the tracker on the lower side since they will not be displaced as much as electrons that enter the magnetic field with lower energies. This gives us an understanding of how changing the size of the tracker lowers the overall acceptance area. For the Electron Ion Collider, the current trackers are set to be a square silicon plate with sides of 20 cm separated 6.76 cm from the $y = 0$ axis, Which also corresponds to the width of the calorimeters directly behind the trackers also giving us the corresponding space that is needed to put the photon detector directly on $y = 0$ axis.

5.3.4 How the beam width affects the acceptance area.

The simulations were done keeping the y vertex of the beam at y=0, meaning that the beam has no width (see figure 28). We want to study how changing adding width to the beam can change the acceptance area and find which parameters need to be changed to take this aspect into consideration.

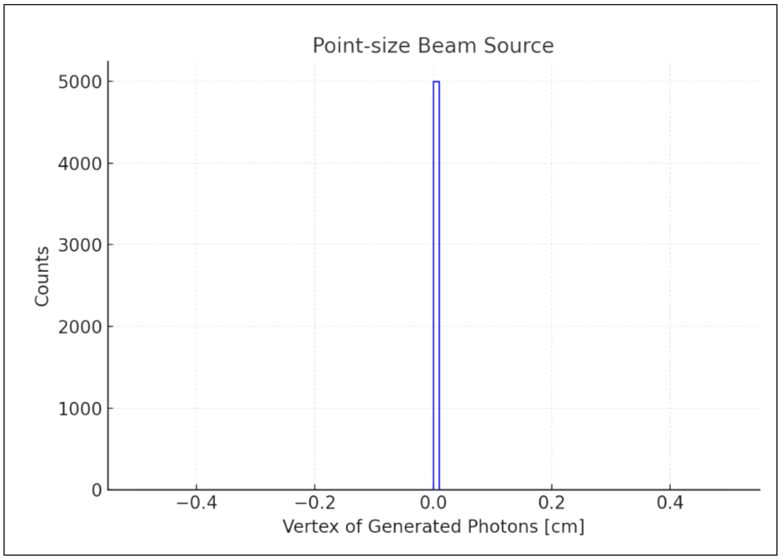

Figure 28: Vertex of the beam (y_{vertex}) where we see that it is a Point-size Beam.

To add width to the beam, we impose a Gaussian distribution on the y component of the vertex, where we have chosen a sigma value of $\sigma = 1.2238cm$; this value is chosen taking into consideration the dimensions of the setup and the definitions inside the geometry files.

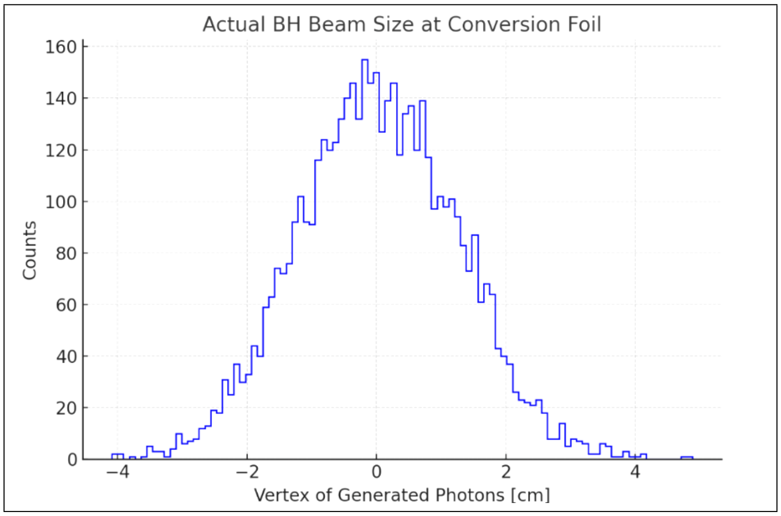

Figure 29: New beam vertex (y_{vertex}) with a Gaussian distribution where $\sigma = 1.2238$ cm.

After adding the beam width, we can now proceed to generate the fiducial areas to check how adding the parameter changes the results.

Firstly, we would like to check how the acceptance area changes with respect to the initial y value of the electron, which is done by adding the shift in y in equations 9 and 10 and creating a new y_o value at different sigmas from the beam.

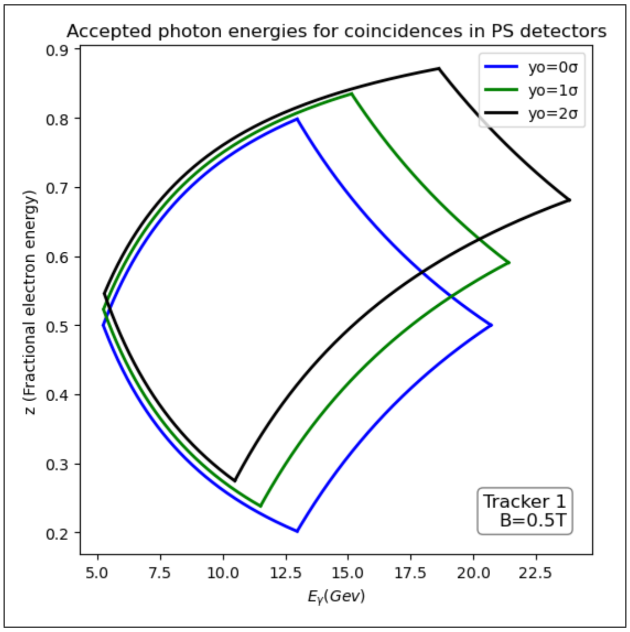

Figure 30: Acceptance Area for positive σ values

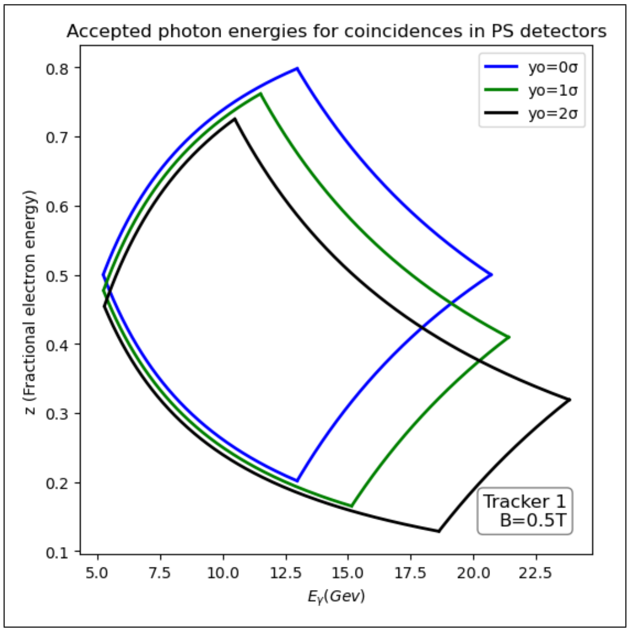

Figure 31: Acceptance Area for negative σ values

From the results, we see a clear change in the acceptance curve where shifting y_0 deforms this area, making it admit larger values of photon energy but decreasing the acceptance in the lower section of the curve. It is also evident that the shapes of the curves generated with positive σ values directly match those with negative σ values, which is the expected behavior if the y_{vertex} is a Gaussian distribution.

Another important point to add is that the overall area of the shape is constant with the change of y, meaning that although the acceptance curve is changing the area contained in it does not vary. This property of the fiducial area is directly related to the dimensions of the tracker, meaning that although we change the original starting position of the electrons, the acceptance area is generated with the entire extent of the tracker. The plots were generated using Tracker 1, which is at a distance $l = 3.89$ m from the dipole magnet and a magnetic field of 0.5 T. Also, by using the trapezoid method, we found the area to be constant inside the curve with a value of $Area = 0.12765$.

Proceeding with the analysis, we want to look at how the area under the curve behaves. This is done by using the trapezoid rule to obtain a value for the area inside the curve for every value of photon energy and plotting this value with respect to the photon energy.

This generates acceptance curves similar to those in figures 19-21, where the location of the peak on the blue curve ($y_0 = 0\sigma$) and the curve in figure 20 are almost identical.

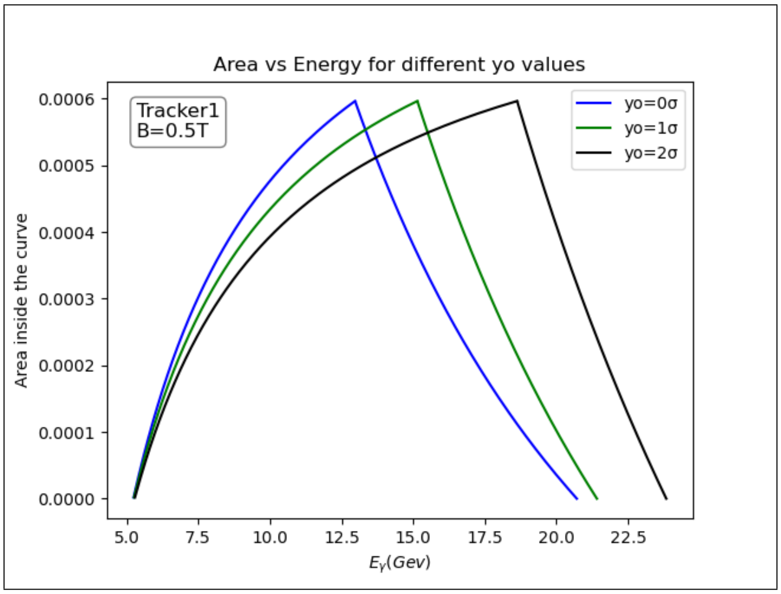

Figure 32: Acceptance Area for positive σ values

The curves show that by moving the y_0 value while keeping the starting position of the curve the same but shifting the rest of the curve, the photon energy that produces the peak is also shifted and the curve admits greater values of E_γ. This is the expected behavior, as when we move the electron further away from the origin, trajectories with higher energy that could not enter the tracker before will now be admitted. This is shown in Figure 32, where we see how the trajectories created by a given energy can enter the tracker depending on its initial position. This is true for both the top and bottom trackers, therefore, overall increasing the acceptance for higher energy electrons.

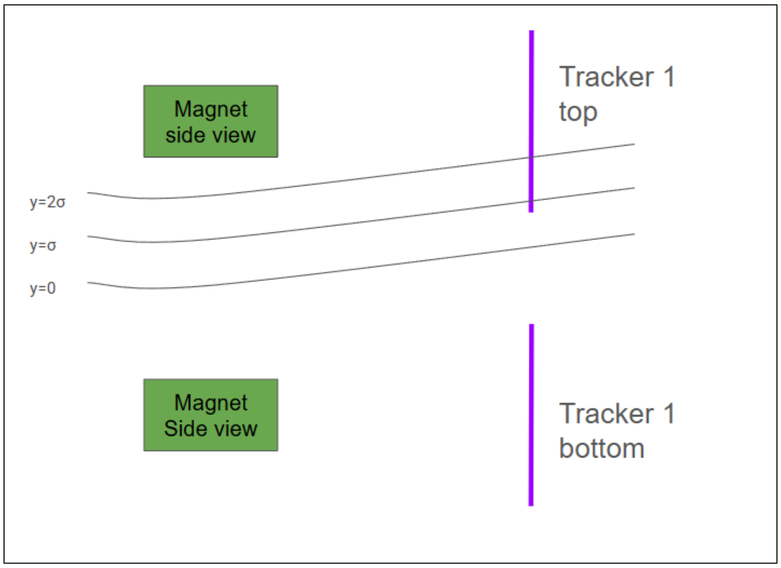

Figure 33: Electron trajectories for different y values.

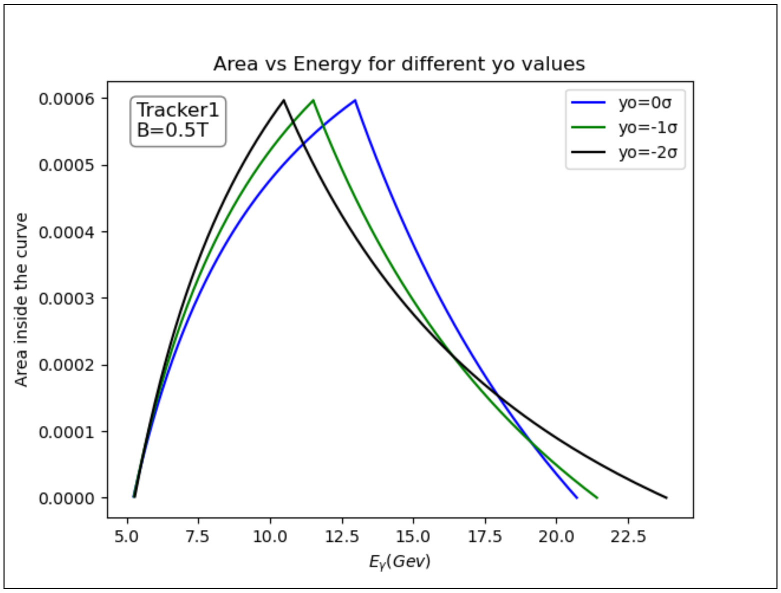

Figure 34: Acceptance Area for negative σ values.

The same behavior is shown for the negative y_0 values, where now the peak is moved toward the left instead of the right. Notice that even if the peaks are moved toward the left, ultimately the green and blue curves will admit higher values of E_γ.

It is also important to redo the simulations, incorporating the new width of the beam, and checking if the behavior correlates with the results shown.

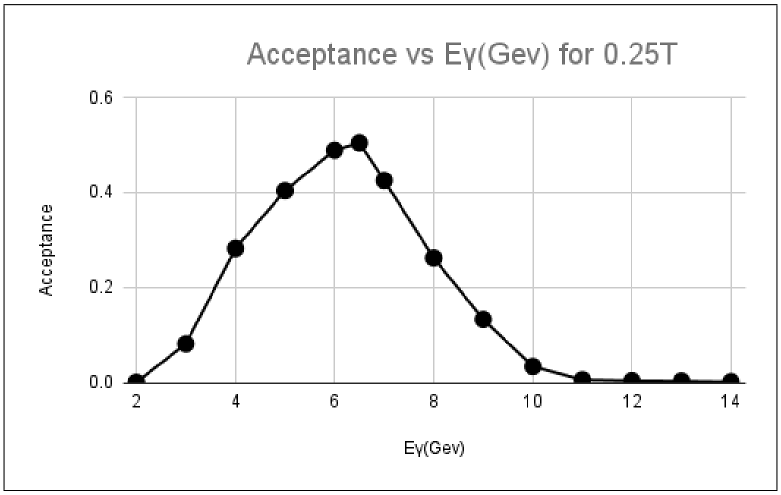

Figure 35: Acceptance Area for a field of 0.25 T with a gaussian distribution for the y_{vertex}

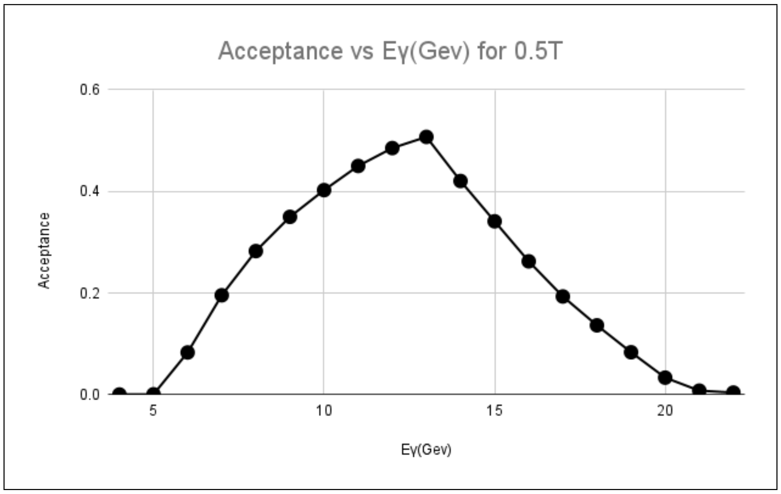

Figure 36: Acceptance Area for a field of 0.5 T with a gaussian distribution for the y_{vertex}

We see that the overall shape of the curves in figures 35,36 is the same as those shown in figures 19,20. The starting point or the minimum value for photon energy admitted is the same, which correlates to the shown in this section; the peak is not displaced as much as expected, which could be because of the gaussian distribution, meaning that the positive and negative σ values are symmetric ending in what appears no displacement of the peaks. The last part of the curves, however does have a change, particularly let us look at the 0.5T curve, where for example, the data points corresponding the energy values of 19 GeV, 20 GeV and 21 GeV have an acceptance of 0.0834, 0.0334 and 0.0078 respectively; in contrast these same data points for the curve shown in figure 20 are 0.0768 for 19 GeV, 0.0338 for 20 GeV and 0.0054 for 21 GeV. Meaning that we gain more acceptance at higher photon energies, which is the behavior shown in figures 31 and 33. Although the values seem small, they represent a great difference when considering the number of events that will be generated at the Electron Ion Collider. Note also that we did not consider the 0.75 T magnetic field for this section. This is because, as shown in the previous sections, this magnitude of magnetic field is not ideal for the current setup.

5.4 Acceptance for the desired bremsstrahlung beams.

The most important aspect of this research is to accommodate the acceptance curves in order to fit the photon energies that will be in the Electron Ion Collider. The energies to take into consideration are those that are contained in the Bethe-Heitler distribution for beams of 5 GeV, 10 GeV, and 18 GeV, which correspond to the bremsstrahlung beams that are expected in the experiment. We will now generate the Bethe-Heitler distributions using Monte Carlo simulations and plot them with the acceptance curves in order to see which magnetic field magnitude is currently the most optimal.

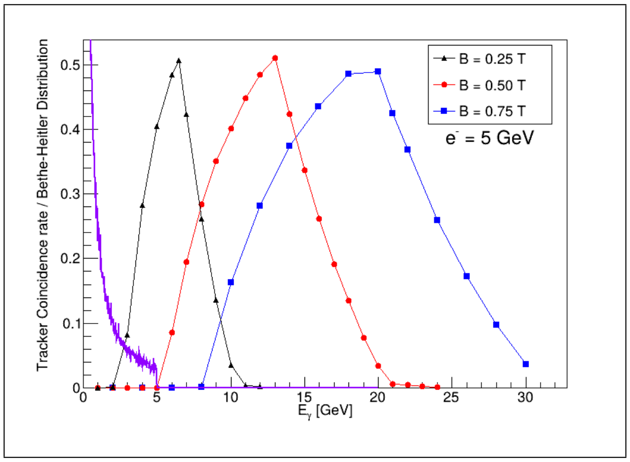

Figure 37: Acceptance Areas with a 5 GeV electron beam Bethe-Heitler distribution

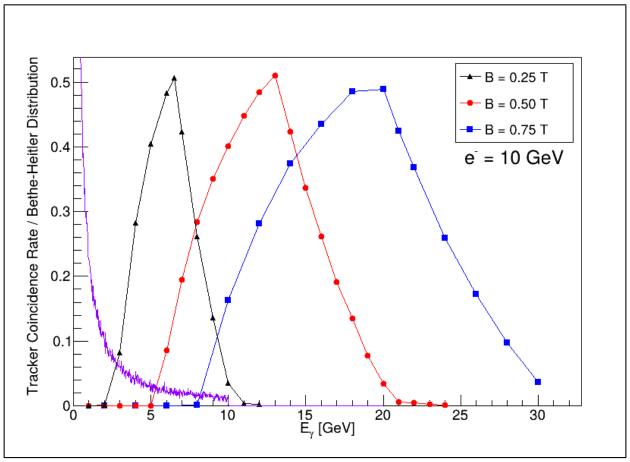

Figure 38: Acceptance Areas with a 10 GeV electron beam Bethe-Heitler distribution

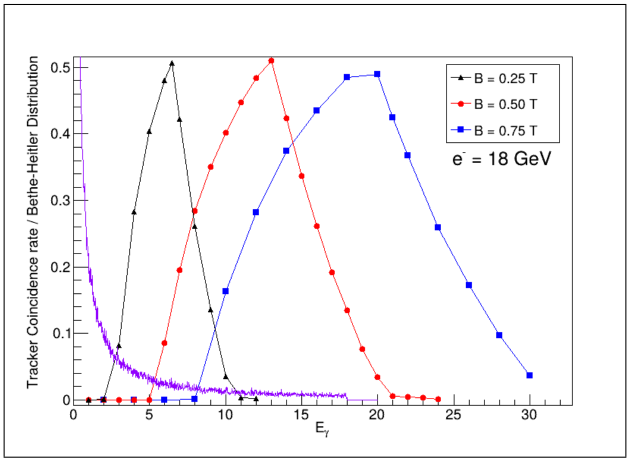

Figure 39: Acceptance Areas with a 18 GeV electron beam Bethe-Heitler distribution

Some conclusions that can be made from the figures 38 and 39 is that with the current dimensions and setup of the trackers a magnetic field of 0.25 T in the dipole magnet is the most ideal, this is because it contains most of the Bethe-Heitler distributions inside it, where the 5 Gev beam ends directly inside the curve, similar to the 10 Gev beam which and a great portion of the 18 Gev beam is also included in the area. Another conclusion we can make is that in order to optimize the setup for the 0.5 T magnetic field, we would need to vertically displace the trackers, for example, a displacement of 1 cm would allow us to lower our energy threshold such that we could gain more acceptance for the 5 GeV Bethe-Heitler beam while also keeping the 18 GeV beam within the fiducial area, but a 5 cm displacement, would decrease the high energy threshold by almost 6 GeV. In contrast, this could also be done for the 0.75 T setup, however, the amount of displacement that could be needed does not match the amount of space we might have at the experiment.

Finally, it is also important to know that using the same magnetic field for the three beams is not necessarily a requirement; currently there are discussions within the group to be able to use different magnetic fields for each one of the beams, making sure we can more accurately optimize the dipole field needed to increase the acceptance for each distribution.

6 Conclusions

During the development of this thesis, numerous skills have been improved and created, from the implementation of different toolkits such as dd4hep to improving the ability to use ROOT and generate coding scripts using Python. It was also crucial to get comfortable using the vast number of files, algorithms, and coding languages used to simulate such a complex experiment as the Electron Ion Collider. All of the simulations were done in a Linux environment. Overall, the ability to generate and understand code was enhanced, creating a solid set of skills that are required in a research environment.

Regarding the research and analysis completed in this thesis. It is critical to understand the behavior of the acceptance curves to be able to generate luminosity measurements inside the EIC, since this represents an important aspect of understanding the physics occurring inside the experiment. It is also valuable that after the culmination of this thesis, a set of scripts and algorithms has been created such that they can be implemented if any changes are needed. Since the EIC is currently in its pre-build stage, parameters inside the definitions and the dimensions are constantly changing, making it important to be able to recreate this analysis with any changes that could be made, the number of trackers, their position, and size, the magnitude and location of the magnetic field, and the vertical displacement needed to generate better acceptance are all variables that can easily be changed in the set of scripts developed such that generating results for these new requirements is not as lengthy.

Some of the properties that we have understood are how the acceptance curve behaves with respect to a change in the tracker size, specifically how the lower portion of the tracker is related to the acceptance of the higher energy electrons, and the opposite is true for the upper side of the tracker. The Acceptance area changes with respect to the distance from the tracker, mainly the different curves for the position of the first and second tracker and the calorimeter. How the change of the magnetic field inside the dipole field changes the size of the acceptance area, as seen in Figure 25. And finally, what we can expect from electrons whose trajectory does not start at $y = 0$ and the behavior of a more realistic beam with a width represented by a Gaussian distribution, showing us how the implementation of this aspect allows us to reach more acceptance at higher energy values.

Finally, this analysis will be extended in the future, as mentioned in the ”Acceptance for the desired bremsstrahlung beams” section, the luminosity group expressed no constraint in having a constant magnetic field for every bremsstrahlung beam, meaning that the next step to complete will be to find an optimal acceptance rate and ideal magnetic field inside the dipole magnet such that this rate is constant across the different bremsstrahlung beams.

Bibliography

[1] Aaron, F., Abramowicz, H., Abt, I., Adamczyk, L., Adamus, M., Al-Daya, M., Alexa, C., Andreev, V., Antonelli, S., Antonioli, P., Antonov, A., Antunović, B., Arneodo, M., Aushev, V., Bachynska, O., Backovic, S., Baghdasaryan, A., Bamberger, A., Barakbaev, A., and Zotkin, D. Combined measurement and qcd analysis of the inclusive e(+/-)p scattering cross sections at hera. *Journal of High Energy Physics* (01 2010).

[2] Abdul Khalek, R., and et. al. Science requirements and detector concepts for the electron-ion collider: Eic yellow report. *Nuclear Physics A 1026* (2022), 122447.

[3] DD4hep authors. *DD4hep User Manual*, 2025. Accessed: 2025-04-01.

[4] Helbich, M., Ning, Y., Paganis, S., Ren, Z., Schmidke, W., Sciulli, F., Schneekloth, U., Büttner, C., Caldwell, A., and Sutiak, J. The spectrometer system for measuring zeus luminosity at hera. *Nuclear Instruments and Methods in Physics Research A 565* (2006), 572–588.

[5] Khalek, R. A., D'Alesio, U., Arratia, M., Bacchetta, A., Battaglieri, M., Begel, M., Boglione, M., Boughezal, R., Boussarie, R., Bozzi, G., Chekanov, S. V., Celiberto, F. G., Chirilli, G., Cridge, T., Cruz-Torres, R., Corliss, R., Cotton, C., Davoudiasl, H., Deshpande, A., Dong, X., Emmert, A., Fazio, S., Forte, S., Furletova, Y., Gal, C., Gwenlan, C., Guzey, V., Harland-Lang, L. A., Helenius, I., Hentschinski, M., Hobbs, T. J., Hoeche, S., Hou, T. J., Ji, Y., Jing, X., Kelsey, M., Klasen, M., Kang, Z. B., Kovchegov, Y. V., Kumar, K. S., Lappi, T., Lee, K., Lee, Y. J., Li, H. T., Li, X., Lin, H. W., Liu, H., Liu, Z. L., Liuti, S., Lorce, C., Lunghi, E., Marcarelli, R., Magill, S., Makris, Y., Mantry, S., Melnitchouk, W., Mezrag, C., Moch, S., Moutarde, H., Mukherjee, S., Murgia, F., Nachman, B., Nadolsky, P. M., Nam, J. D., Neill, D., Neill, E. T., Nocera, E., Nycz, M., Olness, F., Petriello, F., Pitonyak, D., Platzer, S., Prestel, S., Prokudin, A., Qiu, J., Radici, M., Radhakrishnan, S., Sadofyev, A., Rojo, J., Ringer, F., Salazar, F., Sato, N., Schenke, B., Schlichting, S., Schweitzer, P., Sekula, S. J., Shao, D. Y., Sherrill, N., Sichtermann, E., Signori, A., Simsek, K., Simonelli, A., Sznajder, P., Tezgin, K., Thorne, R. S., Tricoli, A., Venugopalan, R., Vladimirov, A., Vicini, A., Vitev, I., Wiegand, D., Wong, C. P., Xie, K., Zaccheddu, M., Zhao, Y., Zhang, J., Zheng, X., and Zurita, P. Snowmass 2021 white paper: Electron ion collider for high energy physics, 2022.